J. Fluid Mech. (1998), *vol.* 375, *pp.* 113–141. Printed in the United Kingdom

Turbulent mixing by breaking gravity waves

By ANDREAS DÖRNBRACK

DLR Oberpfaffenhofen, Institut für Physik der Atmosphäre, D-82230 Wessling, Germany

(Received 4 July 1996 and in revised form 10 July 1998)

The characteristics of turbulence caused by three-dimensional breaking of internal gravity waves beneath a critical level are investigated by means of high-resolution numerical simulations. The flow evolves in three stages. In the first one the flow is two-dimensional: internal gravity waves propagate vertically upwards and create a convectively unstable region beneath the critical level. Convective instability leads to turbulent breakdown in the second stage. The developing three-dimensional mixed region is organized into shear-driven overturning rolls in the plane of wave propagation and into counter-rotating streamwise vortices in the spanwise plane. The production of turbulent kinetic energy by shear is maximum. In the last stage, shear production and mechanical dissipation of turbulent kinetic energy balance.

The evolution of the flow depends on topographic parameters (wavelength and amplitude), on shear and stratification as well as on viscosity. Here, only the implications of the viscosity for the instability structure and evolution in terms of the Reynolds number are considered. Smaller viscosity leads to earlier onset of convective instability and overturning waves. However, viscosity retards the onset of smaller-scale three-dimensional instabilities and leads to a reduced momentum transfer to the mean flow below the critical level. Hence, the formation of secondary overturning rolls is sustained by lower viscosity.

The budgets of total kinetic and potential energies are calculated. Although the domain-averaged turbulent kinetic energy is less than 1% of the total kinetic energy, it is strong enough to form a patchy and intermittent turbulent mixed layer below the critical level.

1. Introduction

Breaking gravity waves exert a significant drag on the atmospheric flow. Knowledge of their locations and magnitude is essential for parameterizing drag in numerical models predicting weather or climate. Current theoretical and computational studies of momentum and mass transfer in stably stratified flows focus mainly on providing useful parameterizations of this effect (see for example Bacmeister *et al.* 1994; Kim & Arakawa 1995; Broad 1995; Shutts 1995). In addition, small-scale mixing by breaking gravity waves in the free atmosphere influences the horizontal and vertical distributions of constituents, e.g. exhaust gases from high flying aircraft (Schumann *et al.* 1995; Schilling & Etling 1996; Dörnbrack & Dürbeck 1998). Furthermore, microphysical and chemical calculations require a knowledge of the small-scale thermal and dynamical structure of internal gravity waves that lead to moisture and temperature conditions which promote the nucleation and growth of aerosol particles (Peter *et al.* 1995; Carslaw *et al.* 1998*a*, *b*).

In the present paper, the life-cycle of vertically propagating internal gravity waves trapped by a critical level is simulated. The high-resolution numerical simulations are restricted to idealized flow conditions where a linear shear flow over a sinusoidal surface excites internal gravity waves in a stably stratified flow. The critical level (the height where the phase speed of a wave equals the mean flow speed) strongly modifies vertical wave propagation: only very small-amplitude waves are transmitted beyond the critical level. Booker & Bretherton (1967) used linear inviscid theory to demonstrate that as a gravity wave propagates through the critical level, its amplitude is reduced by a factor $\exp[-2\pi(Ri_c - 0.25)^{1/2}]$, where $Ri_c > 0.25$ is the Richardson number at the critical level. Beneath the critical level wave energy is absorbed by mean flow. Depending on the wave energy, shear and stratification of the basic flow, turbulence can be generated which cascades kinetic energy to smaller scales. A summary of recent theoretical approaches to the critical level problem can be found in Baines (1995, chapter 4.11).

Worthington & Thomas (1996), who observed the absorption of mountain waves at critical layers by radar on the west coast of Wales, could identify enhanced turbulence beneath the critical layer from the broadening of the spectral width of the radar echo. The wave behaviour below a critical level was studied in the laboratory under well-defined conditions of shear, stability and wave excitation by Thorpe (1981), Koop & McGee (1986), and Delisi & Dunkerton (1989). These mostly qualitative observations are restricted either to flows where the wave energy is small and the flow does not reach overturning or to conditions where three-dimensional structures begin to evolve. So far, measurements of three-dimensional mixed layers after overturning have not been undertaken.

Most numerical investigations of gravity wave–critical layer interaction consider two-dimensional problems (e.g. Fritts 1982; Winters & d'Asaro 1989; Dunkerton & Robins 1992; Schilling & Etling 1996). More recently, Winters & d'Asaro (1994), Dörnbrack, Gerz & Schumann (1995), Fritts, Garten & Andreassen (1996), and Grubišić & Smolarkiewicz (1997) tackled the problem by three-dimensional numerical simulations. Although the wave–mean flow interaction is essentially two-dimensional in its early stage of flow evolution, these latest investigations found fundamently different dynamics of wave instability in three dimensions compared to two-dimensional ones. Winters & d'Asaro (1994) found three-dimensional instability developing by a transverse convective instability of the two-dimensional wave. Fritts *et al.* (1996) drew special attention to flows where the mean shear is at an angle to the direction of wave propagation. For this case, the instability structures are aligned with the background shear flow rather than in the direction of wave propagation. They found less rapid growth compared to the parallel shear flow case. Grubišić & Smolarkiewicz (1997) studied the effect of the critical level on the airflow past an isolated mountain and extended previous studies that were restricted to two-dimensional wave excitation.

Our previous studies have concentrated on two aspects of gravity wave–critical layer interaction. In Dörnbrack & Nappo (1997), results from a two-dimensional version of the numerical code used in the present study were successfully compared with the tank experiment of Thorpe (1981). Because of the limited time of observation due to the finite length of the tilted tube, only results at the early and quasi-linear stage of flow evolution could be considered. Therefore, the present study can be understood as an extension of Thorpe's tank experiment by means of high-resolution numerical modelling for times far beyond the point of first instability. In Dörnbrack *et al.* (1995), the three-dimensional flow evolution using two different formulations of viscosity was investigated: constant viscosity in a direct numerical simulation

(DNS) and flow-dependent viscosity as a function of the local shear perturbation and stability in a large-eddy simulation (LES). Both simulations behave similarly in the early, almost two-dimensional stage of gravity wave–critical level interaction. When the flow becomes nonlinear its structure consists of persistent small-scale overturning waves in the DNS whereas the primary, convectively unstable region collapses rapidly into three-dimensional turbulence in the LES. These results show that convectively overturning regions always form in the same way but the details of subsequent breaking and the resulting structure of the mixed layer depend on the effective Reynolds number of the flow. With sufficient viscous damping, three-dimensional turbulent convective instabilities are more easily suppressed than two-dimensional laminar overturning. From this study it was concluded that the use of a combination of constant and flow-dependent subgrid-scale viscosity is necessary for a correct simulation of the transition from two-dimensional wavy motion to three-dimensional turbulence.

This paper considers flow regimes where the excitation is strong enough to overturn gravity waves and where the net result to be expected is a horizontally homogeneous mixed layer. The main objective of this study is a detailed description of the dynamics and energetics of this three-dimensional breaking. The following questions are to be answered: What are the details of breaking? What is the role of viscosity? What are the characteristics of turbulence generated by breaking gravity waves? How much mean flow energy is transferred to waves, how much to turbulence? Finally, the study should provide fundamental knowledge for the physical understanding of the gravity wave–critical layer interaction and for its parameterization in large-scale models.

The paper is organized as follows. Section 2 briefly reviews the numerical method, describes its initial and boundary conditions, and introduces essential parameters. A detailed description of the gravity wave breaking is given in § 3. Section 4 studies the implications of viscosity on the instability structure and discusses the spectra for flows of different Reynolds numbers. Section 5 investigates the energetics and estimates the mixing efficiency of the breaking process. Similarities and differences between our results and previous, three-dimensional studies are discussed in § 6.

2. Simulation method

The computational method is described in Dörnbrack *et al.* (1995) and here only its essential properties are repeated. The numerical scheme integrates the non-hydrostatic Boussinesq equations in three dimensions and as a function of time:

$$\frac{\partial}{\partial \overline{x}^d}\left(\rho_0 V G^{dq} u_q\right) = 0, \tag{2.1}$$

$$\frac{\partial}{\partial t}\left(V u_i\right) + \frac{\partial}{\partial \overline{x}^d}\left(V G^{dq} u_q u_i\right) = -\frac{1}{\rho_0}\frac{\partial}{\partial \overline{x}^g}\left(V G^{gi} p\right) - \frac{\partial}{\partial \overline{x}^d}\left(G^{ds}\left(V F_{is}\right)\right) + V g \frac{\theta}{\vartheta_0}\delta_{3i}, \quad i = 1, 2, 3. \tag{2.2}$$

Additionally, an equation for the temperature fluctuations

$$\frac{\partial}{\partial t}\left(V\theta\right) + \frac{\partial}{\partial \overline{x}^d}\left(V G^{dq} u_q \theta\right) + V u_3 \frac{\mathrm{d}\Theta}{\mathrm{d}x_3} = -\frac{\partial}{\partial \overline{x}^d}\left(G^{dr}\left(V Q_r\right)\right) \tag{2.3}$$

is solved. The governing equations (2.1) to (2.3) are formulated for the Cartesian coordinates (x, y, z) as a function of curvilinear coordinates $(\overline{x}, \overline{y}, \overline{z})$ according to the

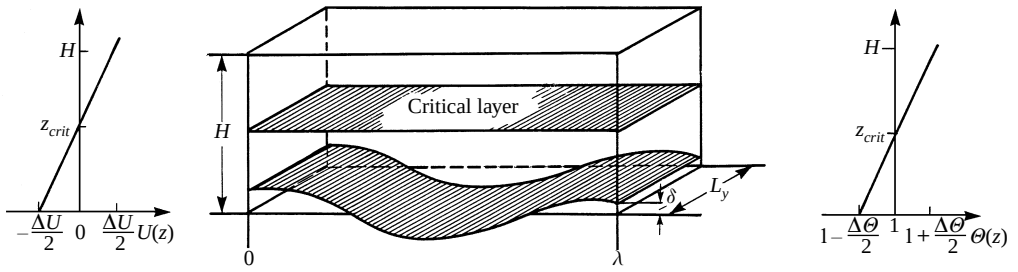

FIGURE 1. Schematic sketch of the computational domain and the model set-up. The critical layer z_{crit} is defined by $U = 0$. The wave amplitude is $\delta = 0.03125\,H$ and the wavelength is $\lambda = 1.5625\,H$. The velocity and temperature differences across the vertical depth H are chosen in such a manner that the bulk Richardson number Ri_B is approximately 1.1 at the beginning.

transformation $\overline{x} = x$, $\overline{y} = y$, $\overline{z} = \eta(x, z)$. The Jacobian of the transformation is $V = \mathrm{Det}[G^{ij}]^{-1}$ with $G^{ij} = \partial\overline{x}_i/\partial x_j$. Here, $\eta(x, z) = H\,(z - h)/(H - h)$ maps the domain above the wavy surface with height $h(x) = \delta \cos k_x x$, where $k_x = 2\pi/\lambda$, and below a plane top surface at $z = H$ into a rectangular transformed domain. The wave amplitude is $\delta = 0.03125\,H$ and the wavelength is $\lambda = 1.5625\,H$. These values are taken from a comparison of our numerical results with the tank experiment of Thorpe (1981), see Dörnbrack *et al.* (1995). Figure 1 shows the computational domain of height H, length λ and width $\lambda/5$.

The governing equations are approximated by finite differences on a staggered grid with $(nx, ny, nz) = (150, 30, 96)$ mesh cells. In the horizontal directions the grid spacing is equidistant ($\Delta x = \Delta y = H/nz$). A higher resolution close to the critical level is achieved by transforming the vertical coordinate η on a non-equidistant grid using

$$\eta_k^* = \frac{H}{2}\left\{\alpha \sinh\left[\mathrm{arcsinh}(\alpha^{-1})\left(2\,\frac{k-1}{nz} - 1\right)\right] + 1\right\}, \quad k = 1, 2, \ldots, nz + 1. \tag{2.4}$$

The parameter $\alpha = 0.1$ is chosen so that the grid spacing is reduced by one order of magnitude from its surface value to the value at the critical level.

The diffusive fluxes in (2.2) and (2.3) are calculated by means of a first-order closure

$$VF_{ij} = -K_M\,V2\,D_{ij}, \quad VQ_i = -K_H\,\frac{\partial}{\partial\overline{x}^r}\left(VG^{ri}\theta\right), \tag{2.5}$$

where the deformation tensor D_{ij} in terrain-following coordinates reads

$$D_{ij} = \frac{1}{2}\,\frac{1}{V}\,\frac{\partial}{\partial\overline{x}^r}\left(VG^{rj}u_i + VG^{ri}u_j\right). \tag{2.6}$$

The subgrid-scale diffusivities K_M and K_H are modelled as the sum of a uniform and a flow-dependent eddy viscosity according to

$$K_M = \frac{1}{Re} + \nu_{turb} \quad \text{and} \quad K_H = \frac{1}{RePr} + \frac{\nu_{turb}}{Pr_{turb}}, \tag{2.7}$$

with $Re = \Delta U H/\nu_M$ and $Pr = \nu_M/\gamma$. The velocity difference across the vertical depth H is ΔU, ν_M denotes the kinematic viscosity, γ is the thermal conductivity, and $Pr_{turb} = 1$. For this subgrid-scale model different Reynolds numbers $Re = 2 \times 10^4$, 3×10^4, and 5×10^4 are tested. For the simulation presented in § 3 we take $Re = 5 \times 10^4$ as the flow evolution becomes nearly insensitive to further small changes of Re. Based

on suggestions by Lilly (1962) and Schumann (1975), the turbulent viscosity

$$\nu_{turb} = \begin{cases} \Lambda^2 |S - \overline{S}|(1 - Ri/Ri_c)^{1/2}, & Ri < Ri_c = 1 \\ 0, & \text{otherwise,} \end{cases} \tag{2.8}$$

is determined by the local values of shear perturbation $S' = |S - \overline{S}|$ and as a function of the local Richardson number

$$Ri = \frac{g}{\vartheta_0} \frac{\partial \vartheta / \partial z}{\left(\partial u/\partial z\right)^2 + \left(\partial v/\partial z\right)^2}. \tag{2.9}$$

The quantity $S = (2D_{ij}D_{ij})^{1/2}$ denotes the second invariant of the deformation tensor and $\overline{S} = \Delta U/H$ is the mean vertical shear. The mixing scale Λ is related to the grid spacings as $\Lambda = 0.1(\Delta x + \Delta y + \Delta z)/3$. In (2.8), $\nu_{turb} \neq 0$ is restricted to regions of wave–critical layer interaction, i.e. closely beneath the critical layer where the deformation of $U(z)$ is strongest and where Ri drops significantly below its critical value Ri_c. The total temperature

$$\vartheta(\boldsymbol{x}, t) = \vartheta_0 + \Theta(z) + \theta(\boldsymbol{x}, t) \tag{2.10}$$

consists of three components: a constant reference temperature ϑ_0, the linear background stratification according to

$$\frac{\Theta(z)}{\vartheta_0} = \frac{\Delta\Theta}{\vartheta_0} \frac{(z - 0.5H)}{H}, \quad \text{where} \quad \frac{\Delta\Theta}{\vartheta_0} = \frac{N^2 H}{g}, \tag{2.11}$$

and finally the fluctuations $\theta(\boldsymbol{x}, t)$. The Brunt–Väisälä frequency N and the mean shear $\overline{S}$ are chosen is such a way that the bulk Richardson number $Ri_B = N^2/\overline{S}^2$ is approximately 1.1 at the beginning.

The initial velocity distribution equals $U(z) = \overline{S}\,(z - 0.5H)$, i.e. the fluid speed is zero at $z = 0.5\,H$ (see figure 1). The flow over the sinusoidal surface excites gravity waves with zero phase speed and, hence, their critical layer is situated at midheight. Initially, the flow is disturbed by small random temperature perturbations, otherwise it would remain two-dimensional for all times. Cyclic boundary conditions are used in the streamwise (x) direction and in the spanwise (y) direction. The boundaries at the lower and upper wall are free-slip and adiabatic as described in Dörnbrack *et al.* (1995). In the following, all quantities are normalized by the velocity, length, temperature, density, and time scales ΔU, H, ϑ_0, ρ_0, and $t_{ref} = H/\Delta U$, respectively. The simulations stop at $t = 75$, where the flow has reached a steady state in the budget of the turbulent kinetic energy. Details of the numerical implementation can be found in Krettenauer & Schumann (1992).

3. Flow structure

In this section, we give an overview of the temporal evolution of the breaking internal gravity waves below a critical level for $Re = 5 \times 10^4$. Tests have shown that the flow evolution is nearly insensitive to a further increase of Re: this run represents typical characteristics of the turbulent breakdown. Figure 2 juxtaposes the temporal evolution of the thermal, figure 2 (*a*), and dynamical, figure 2 (*b*), flow structure. Based on the analyses of the simulation results, the flow development can be divided into three stages.

In the first stage ($0 < t < 17$) vertically propagating gravity waves are formed. At $t = 0$, the ϑ-segments are horizontal and equidistant and are only slightly disturbed

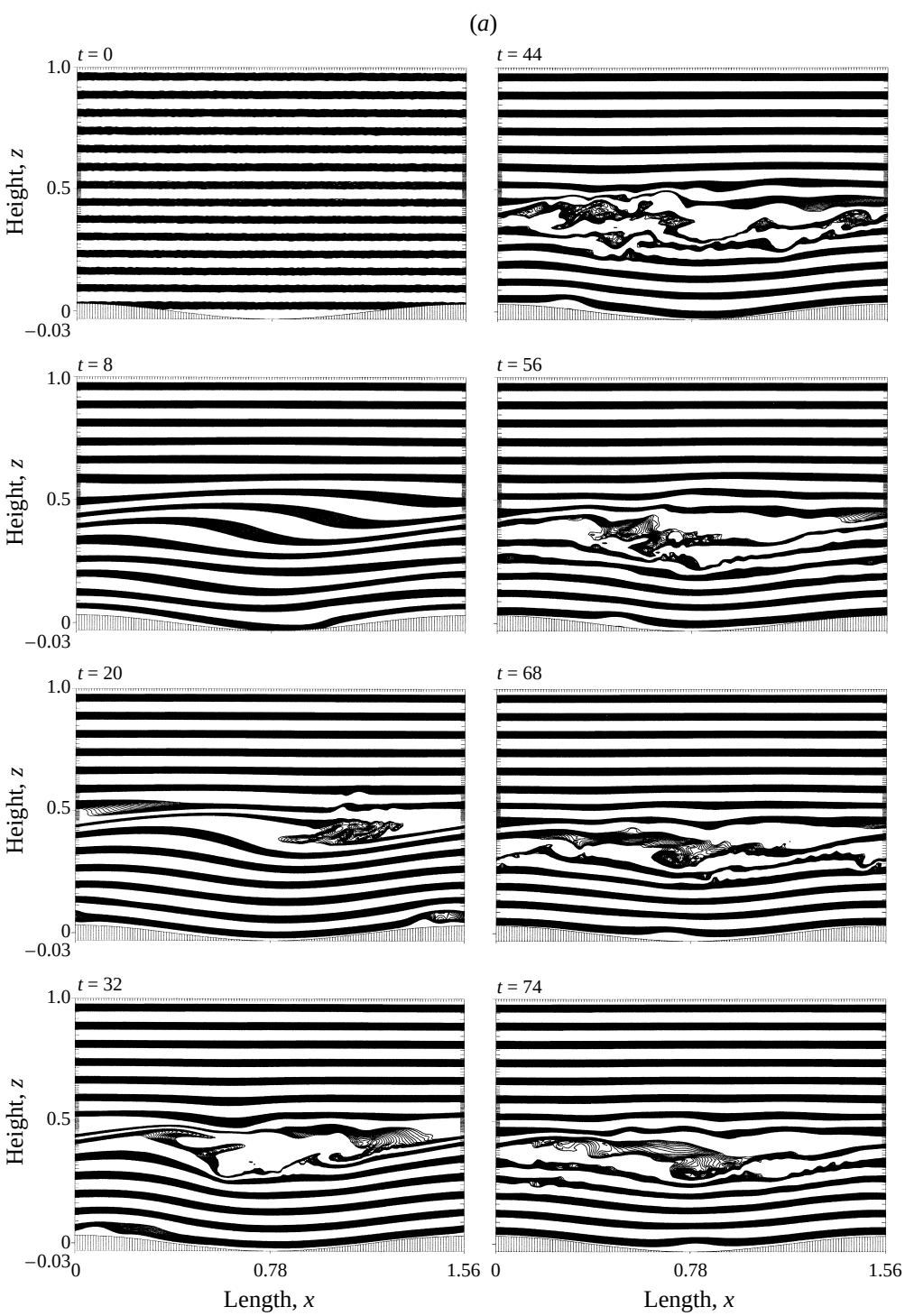

FIGURE 2. For caption see facing page.

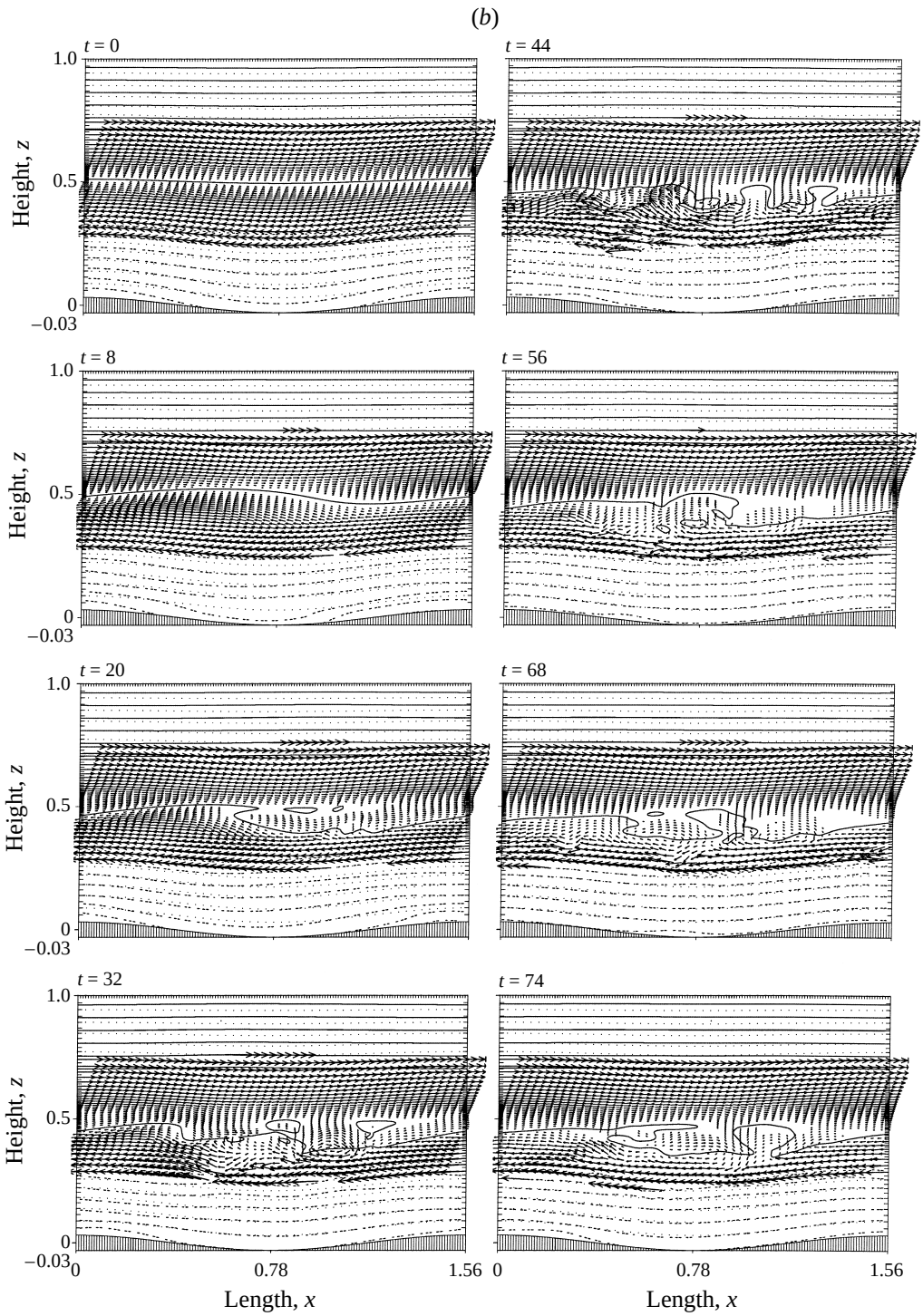

FIGURE 2. (*a*) Instantaneous temperature field ϑ in a vertical plane $y = 0$ as function of time. The thickness of the black segments is $0.002\Delta\Theta$. Broader segments indicate reduced, thinner ones enhanced, thermal stability. (*b*) Streamwise velocity component u at the same times as in (*a*). Negative values are denoted by dashed lines, positive ones by solid lines, the increment is $0.05\,\Delta U$. Superimposed are (u, w)-vectors with a maximum vector length of $0.25\,\Delta U$.

by random perturbations (see figure 2 *a*). Cold fluid is in the trough and the fluid temperature becomes warmer with increasing height. For $t > 0$, the mean flow over the sinusoidal corrugations creates gravity waves. At $t = 8$, figure 2 (*a*) reveals two types of waves: evanescent waves with contour lines in phase with the underlying orography for $z < 0.25$ and internal gravity waves with tilted phase lines above that altitude and below the critical level.

Linear wave theory (e.g. Smith 1979; Gill 1982) can explain this behaviour in terms of the wavenumber ratio $\gamma = k_x/\ell(\eta)$, where $\ell = N/|u(\eta)|$ is the local Scorer parameter (see Scorer 1949 or Eliassen & Palm 1960). If $\gamma > 1$, i.e. if the intrinsic frequency uk_x (the phase speed of the excited waves relative to the topography is zero) is large compared to the Brunt–Väisälä frequency N, buoyancy has little effect on the flow and the streamlines remain in phase with the topography. These waves are called evanescent since their amplitude vanishes exponentially with height. For increasing stability, or similarly for decreasing flow speed, the ratio γ becomes less than one, i.e. the intrinsic frequency uk_x is less than N, and the waves are able to propagate vertically. These waves are called internal gravity waves. For the parameters of the present simulation, internal gravity waves can exist for heights $z > 0.2$ in agreement with results at $t = 8$ shown in figure 2 (*a*).

The amplitude of the upward travelling waves increases with height (up to nearly $3\,\delta$) but falls to zero just below the critical level. No wavy motion is found above this level which suppresses the transmission of gravity waves. Regions of reduced thermal stratification (characterized by a widening of marked segments) are located above the trough of the surface wave. Over the crest, the vertical temperature gradient becomes large, the black and white segments are thinner and adjacent segments narrow. Due to the interaction of the internal gravity wave with its critical level, the plane $u = 0$ descends to the right of the trough ($x > \lambda/2$) and rises to the left of it (see $x < \lambda/2$ in figure 2 *b*). This creates stagnant regions of diminished thermal stability above the trough and a zone of enhanced shear where the thermal stratification is large. The deviation of the instantaneous (u, w)-field from its initial state obviously indicates the change of the flow structure by the wave–mean flow interaction (see figure 3 *a*). The largest increase of u and w occurs above the trough and below the critical level. A similar structure (maximal shear at locations of stable stratification and zero shear at locations of unstable stratification) was found by Winters & Riley (1992). They used WKB-analysis to determine the approximate form of an internal gravity wave approaching its critical level in a shear flow. Generally, the flow remains two-dimensional in this early stage.

In the second stage ($17 < t < 44$), gravity waves gradually raise cold fluid into formerly warm regions just above the trough while warm fluid sinks down into cold regions above the crest of the corrugated surface (figure 2 *a*). The lifted colder fluid moves over warmer fluid in the positive x-direction by wave-induced advection below the critical level. At lower levels, the mean flow slides warm fluid under colder fluid. This process can be understood by inspecting the wavy motion components shown in figure 3 (*b*) (for a definition of the averages see the Appendix). Gravity waves transfer either positive horizontal momentum upwards ($\tilde{u} > 0$ and $\tilde{w} > 0$) or negative momentum downwards ($\tilde{u} < 0$ and $\tilde{w} < 0$). Altogether, the deposit of horizontal momentum accelerates the mean flow above the trough and its removal decelerates the flow above the crest of the surface wave. The long lasting momentum transfer to and from the mean flow generates regions of stagnant fluid in the convectively unstable zone and regions of enhanced shear ('braid'-like zones) above the surface crest. Convective instability occurs suddenly by spontaneous

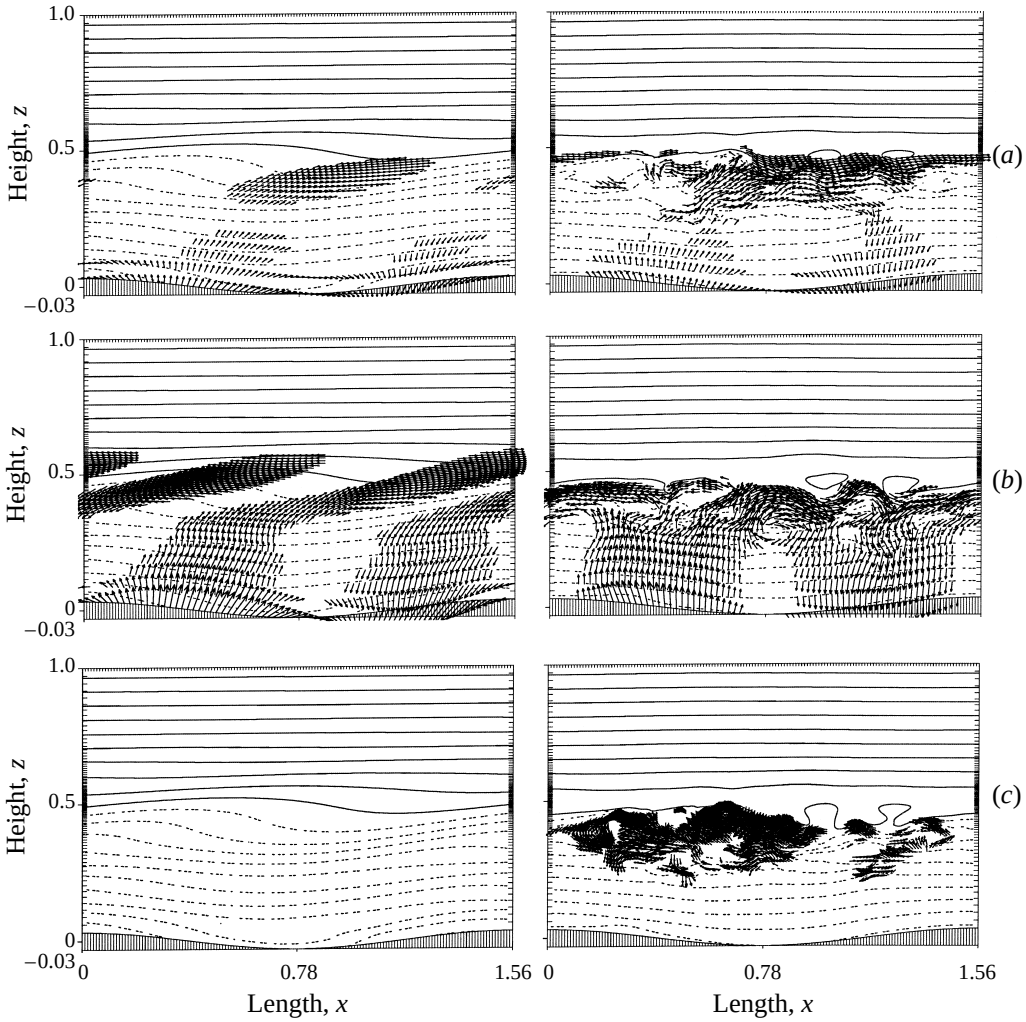

FIGURE 3. Vertical cross-sections of (u, w)-vectors at $t = 8$ (left-hand column) and $t = 44$ (right-hand column): (*a*) deviation of instantaneous velocity field from its initial state $(U(z), 0)$, (*b*) wavy velocity components $(\tilde{u}, \tilde{w})$ (see Appendix for the definition of the average), and (*c*) turbulent velocity components (u'', w''). Contour lines of the instantaneous streamwise velocity field are superimposed on each plane. The maximum vector lengths are 0.2 (*a*), 0.1 (*b*), 0.015 ΔU (*c*).

and explosive breakdown of heavier, i.e. cold, fluid in the region upstream of the surface trough. Approximately three Brunt–Väisälä periods were required for the growth of instability and the transition into three-dimensional motions at $t \approx 17$. Vortical motions with axis in the spanwise direction (rolls) were produced by the convective breakdown (see $t = 20$ in figure 2*a*). The flow above the breaking region is slightly disturbed by spluttering cold fluid parcels. At later times, the restoring force of buoyancy suppresses these disturbances. They do not influence the further flow evolution. Below the critical level, the mean flow advects the mixed region into the negative x-direction, creating a horizontally expanding mixed layer. Moreover, downstream and at its lower edge, a shear layer forms small-scale overturning rolls (see $t = 32$ in figure 2). These shear-induced, secondary rolls continuously entrain

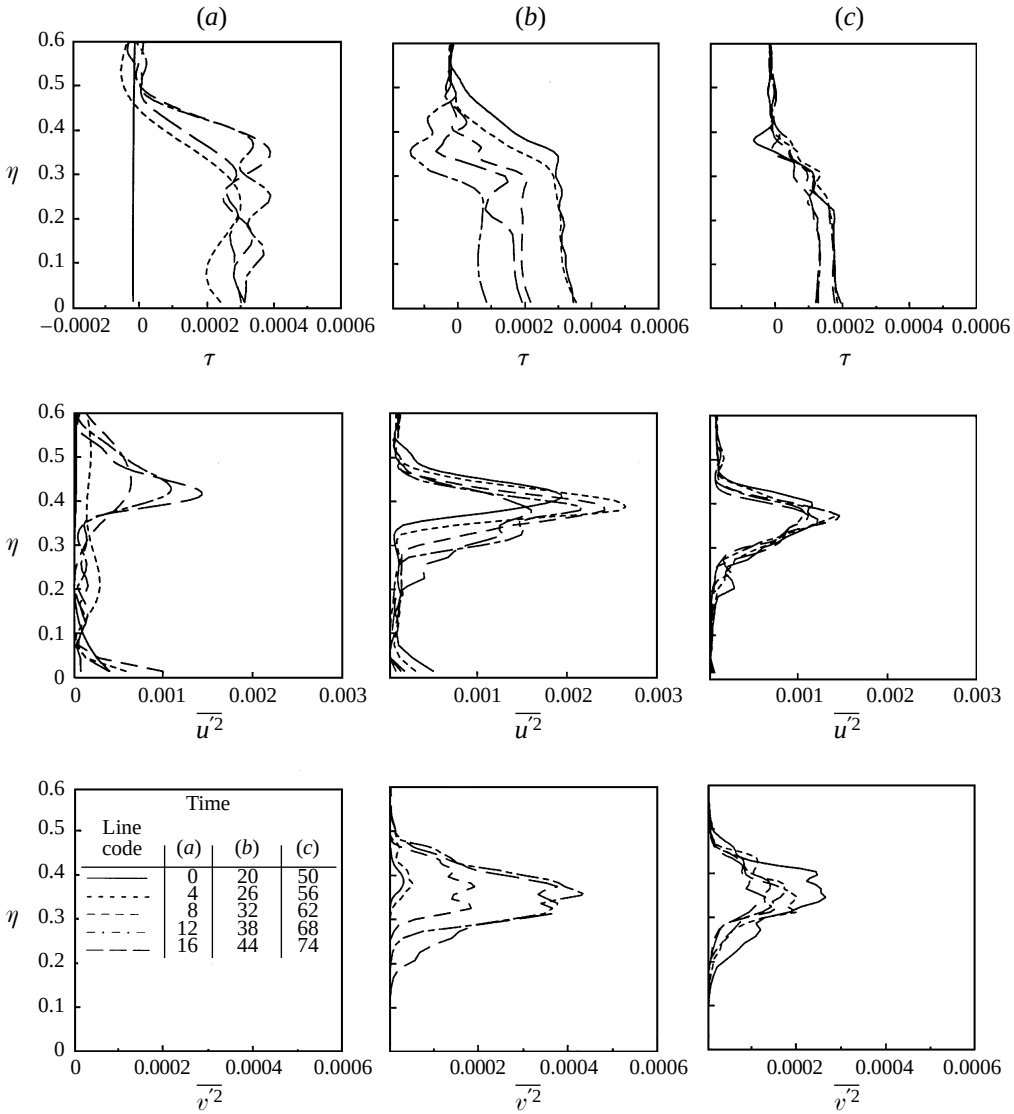

FIGURE 4. Horizontally averaged profiles of the vertical flux of horizontal momentum $\tau = \overline{u'w'}$ (top) and of the horizontal velocity variances $\overline{u'^2}$ (middle) and $\overline{v'^2}$ (bottom) as function of the vertical coordinate η. The three columns comprise curves at different times as shown in the table at lower-left. The colums (*a*), (*b*) and (*c*) are arranged according to the three stages of flow evolution.

colder and higher momentum fluid from below and mix it with warmer upper-level fluid. Thus, the mixed layer spreads over a deep vertical range beneath the critical level.

A quasi-steady state of mixing is reached in the last stage ($t > 44$). The mixed layer consists of shear-induced, small-scale overturning rolls that are advected by the mean flow (see figure 3). In the core of each of these isolated overturning rolls, the local *Ri* is negative which leads to the final patchiness and intermittency of turbulence (see figure 3*c*). Furthermore, the flow consists of organized structures, namely counter-rotating streamwise vortices which will be discussed below.

For each stage of flow evolution, figure 4 shows the momentum flux $\tau = \overline{u'w'}$ and the horizontal velocity variances arranged in three columns. The momentum flux τ is positive and vertically uniform up to $\eta \approx 0.4$ in the first stage. Above this altitude, τ decreases sharply and is zero at the critical level. The positive divergence $-\partial\tau/\partial\eta$ in this layer results in the acceleration $\partial\bar{u}/\partial t > 0$ of the mean flow and the advection of lifted cold fluid over warmer fluid. The u'-variance grows with height, is maximum at $\eta \approx 0.4$ and falls to zero towards the critical level. In this period of flow evolution, the u'-variance grows temporally. The absence of the v'-variance indicates the two-dimensionality of the flow in the first stage. In the second stage, both the u'- and the v'-variances increase rapidly in time and the mixed layer evolves towards full three-dimensionality. The height of maximum variance descends. The flow in the gradually sinking mixed layer is highly anisotropic as the r.m.s. values of v are one order of magnitude smaller than those of u. During the breaking, the momentum flux τ decreases significantly at all levels. In regions of high turbulence τ even becomes negative, i.e. momentum is transported downward (compare figure 12). For $t > 44$, the momentum flux as well as the horizontal velocity variances change only slightly in time exhibiting the quasi-steady state of flow evolution.

The development of streamwise vortices is displayed in figure 5 by a series of lateral cross-sections of the (v, w)-velocities and the local Richardson number Ri at five horizontal locations x_α ($\alpha = 1, \ldots, 5$). Early on, the overturning creates an elongated convectively unstable layer that is seen as a laterally coherent layer of negative Ri ($t = 21.5$ in figure 5*a*). Its vertical depth depends on x and does not exceed $0.2\,H$. Above the crest ($x_5 = \lambda$), this layer appears as an elevated, vertically compressed but laterally essentially homogeneous region. Only weak wave-like disturbances and isolated patches of $Ri < 0$ (due to the eruptive breaking at earlier times) disturb the lateral homogeneity. Downstream, the region of instability thickens and descends (see $x_3 = 0.6\,\lambda$ and $x_4 = 0.8\,\lambda$). In this layer, the shear vanishes and the amplitudes of the three-dimensional velocity components grow rapidly in time. In this way, the lateral homogeneity is no longer sustained and the downward motion of lifted cold fluid leads to adjacent regions of negative and positive vertical velocity and finally to the generation of a pair of counter-rotating vortices. The production of streamwise vorticity is spatially restricted to the locations inside the convective layer (see positions x_2, x_3, and x_4 at $t = 21.5$ and 28.5). Hence, the mechanism of generating streamwise vortices is dominated by buoyancy at this stage of flow evolution. The resulting vortices are aligned in the direction of mean shear and wave propagation. Their magnitude is small compared to that of the spanwise overturning rolls.

At $t = 28.5$, the streamwise vortices have been advected downstream (figure 5*b*). The most interesting process occurs near $x_2 = 0.4\,\lambda$ where the streamwise vortices enter a region of strong vertical transport of horizontal momentum. At this location, overturning rolls entrain high-momentum fluid from below (as discussed in figure 2 for $t = 32$). The penetration through this momentum-flux barrier retards the horizontal expansion of the mixed region. Vertical components of the flow field are produced resulting in a lifting of the mixed layer (figure 5*b*). As a result, streamwise vorticity is created and the three-dimensional mixing extends vertically. In contrast to the downstream advection of counter-rotating streamwise vortices, the wave-induced advection below the critical level to the right of the trough transports vortices in the opposite direction. Above the crest (see positions x_4 and x_5), these vortices narrow and the vertical extent of the unstable layer is significantly reduced.

At later times (see $t = 41.5$, figure 5*c*), the vertical shear over the crest and at the lower edge of the mixed layer is the main mechanism for generating streamwise

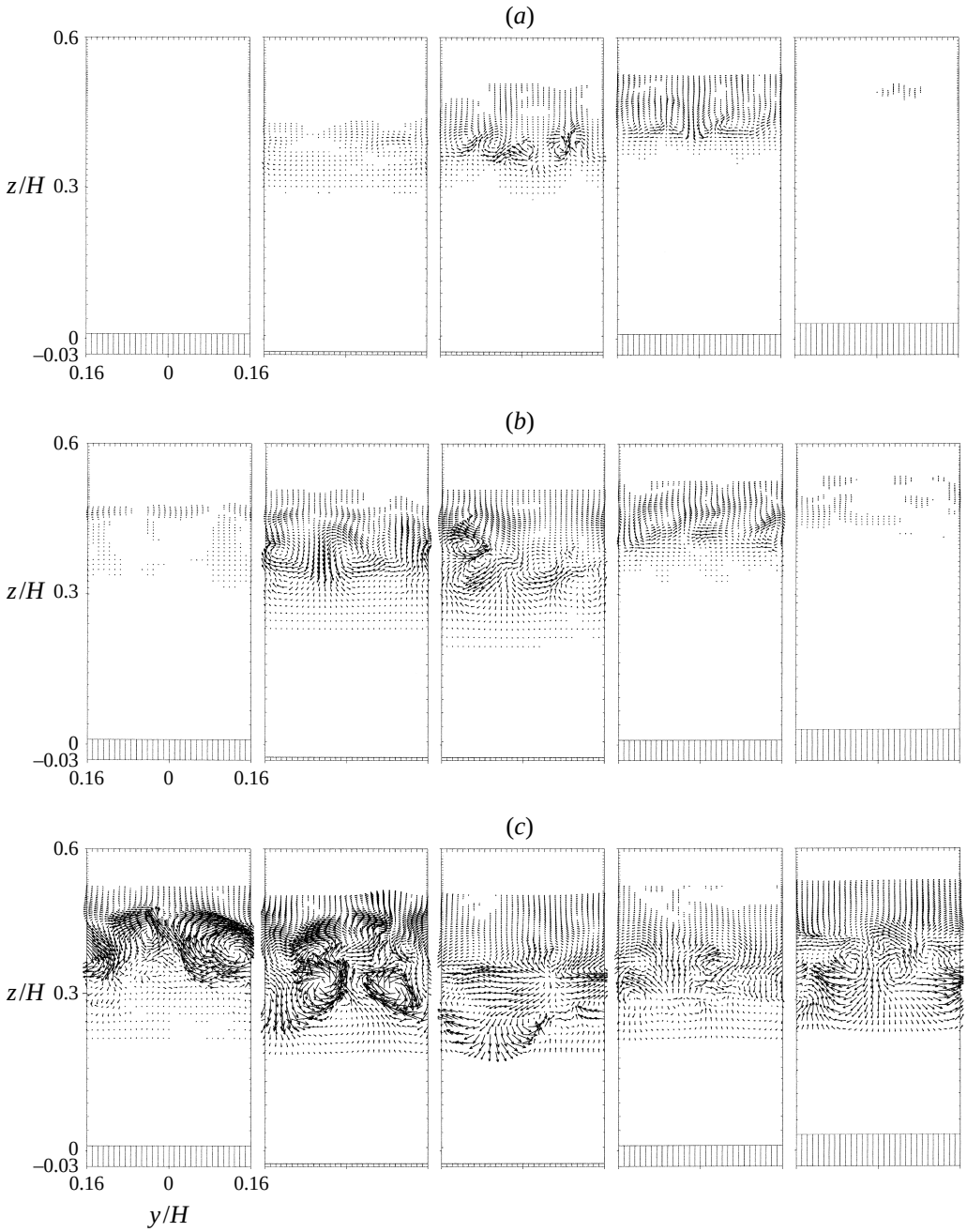

FIGURE 5. For caption see facing page.

vortices. Figure 5(*c*) reveals a turbulent mixed layer extending horizontally over the entire domain. The strongest streamwise vortices appear at positions above the trough. The previously coherent mixed layer has broken up into isolated, tiny patches of negative Richardson number leading to its intermittent character in the late stage.

High-resolution time-series of the instantaneous, unaveraged velocity components u and w, and of the temperature θ represent virtual measurements at every timestep

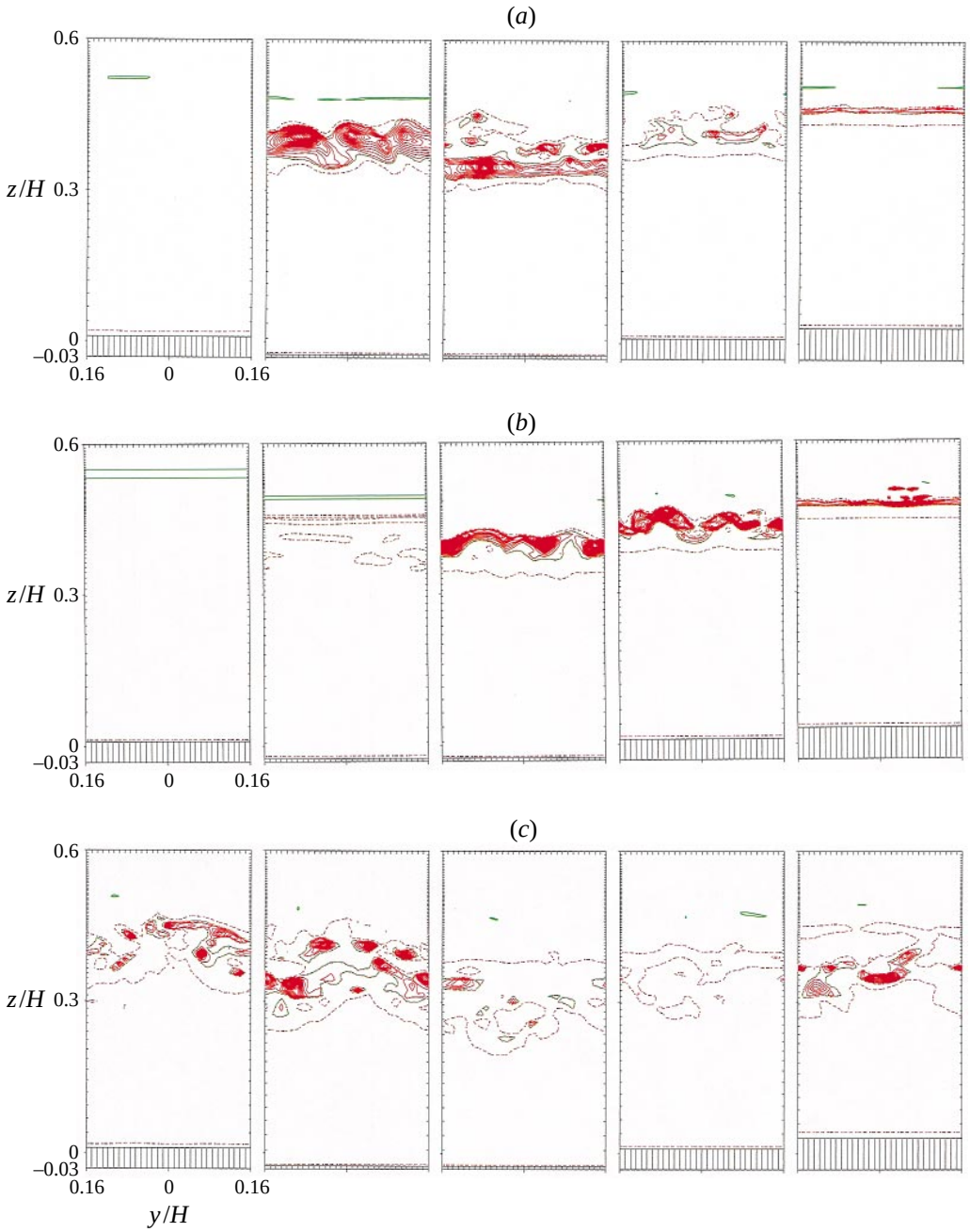

FIGURE 5. Instantaneous velocity field (v, w) (left) and local Richardson number Ri (right) in spanwise sections at $x_\alpha = 0.2\lambda$, 0.4λ, 0.6λ, 0.8λ and λ (from left to right) at (*a*) $t = 21.5$, (*b*) $t = 28.5$, (*c*) $t = 41.5$. The green contour line indicates $Ri = 0$, the dashed one $Ri = 0.25$, and the red lines denote negative Ri.

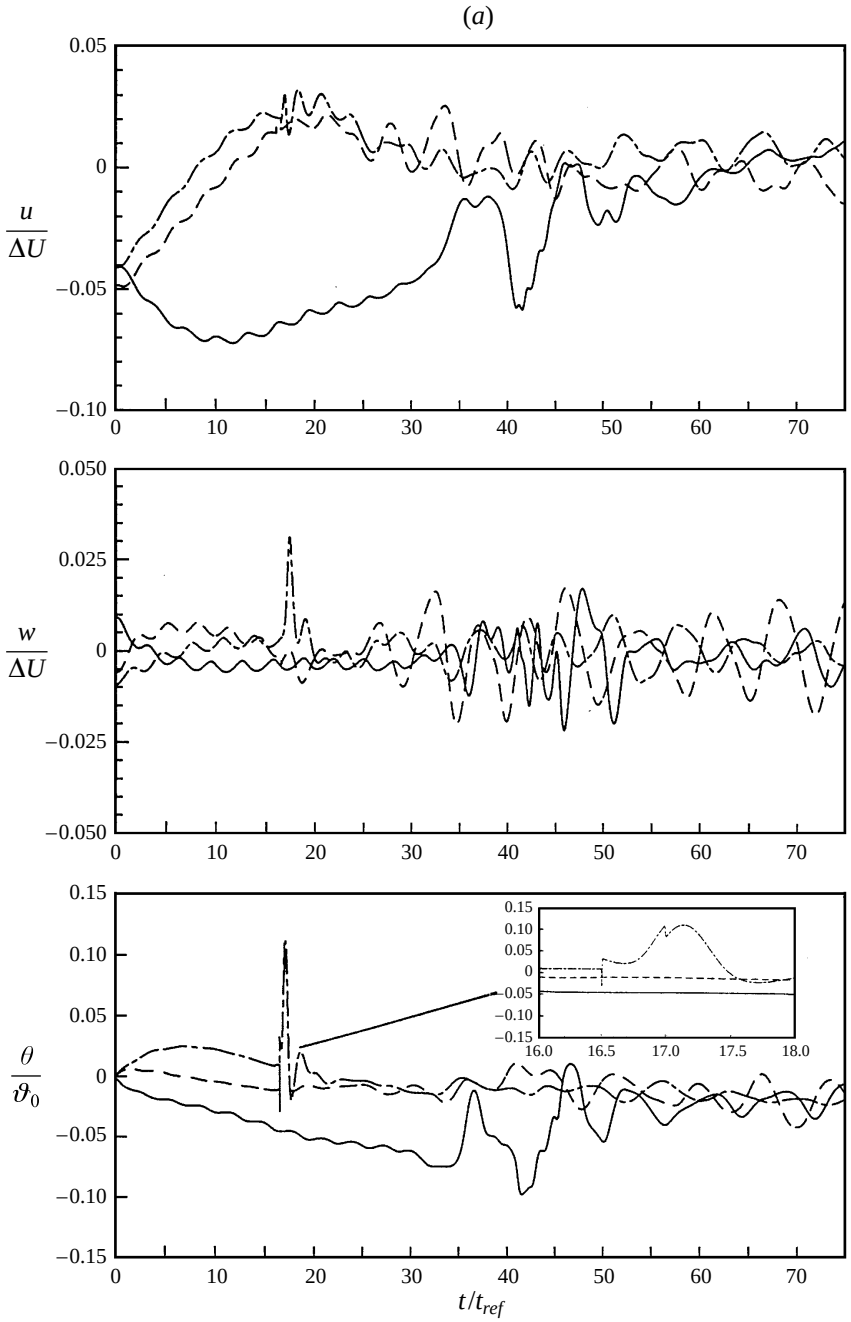

FIGURE 6. For caption see facing page.

by a spatially fixed observer. The results are displayed in figure 6 for two vertical levels at $y = 0$ and at $x = 0.2\,\lambda, 0.6\,\lambda, 0.8\,\lambda$. At early times, the horizontal velocity is slightly negative just beneath the critical level ($\eta \approx 0.46$) due to the initial profile $U(z)$ (see figure 6 *a*). Through the momentum transfer by the wave the local flow is accelerated to the right of the surface trough (at $x = 0.6\,\lambda$ and $0.8\,\lambda$) whereas it is decelerated at $x = 0.2\,\lambda$. The maximum velocity increase δU is approximately 0.07

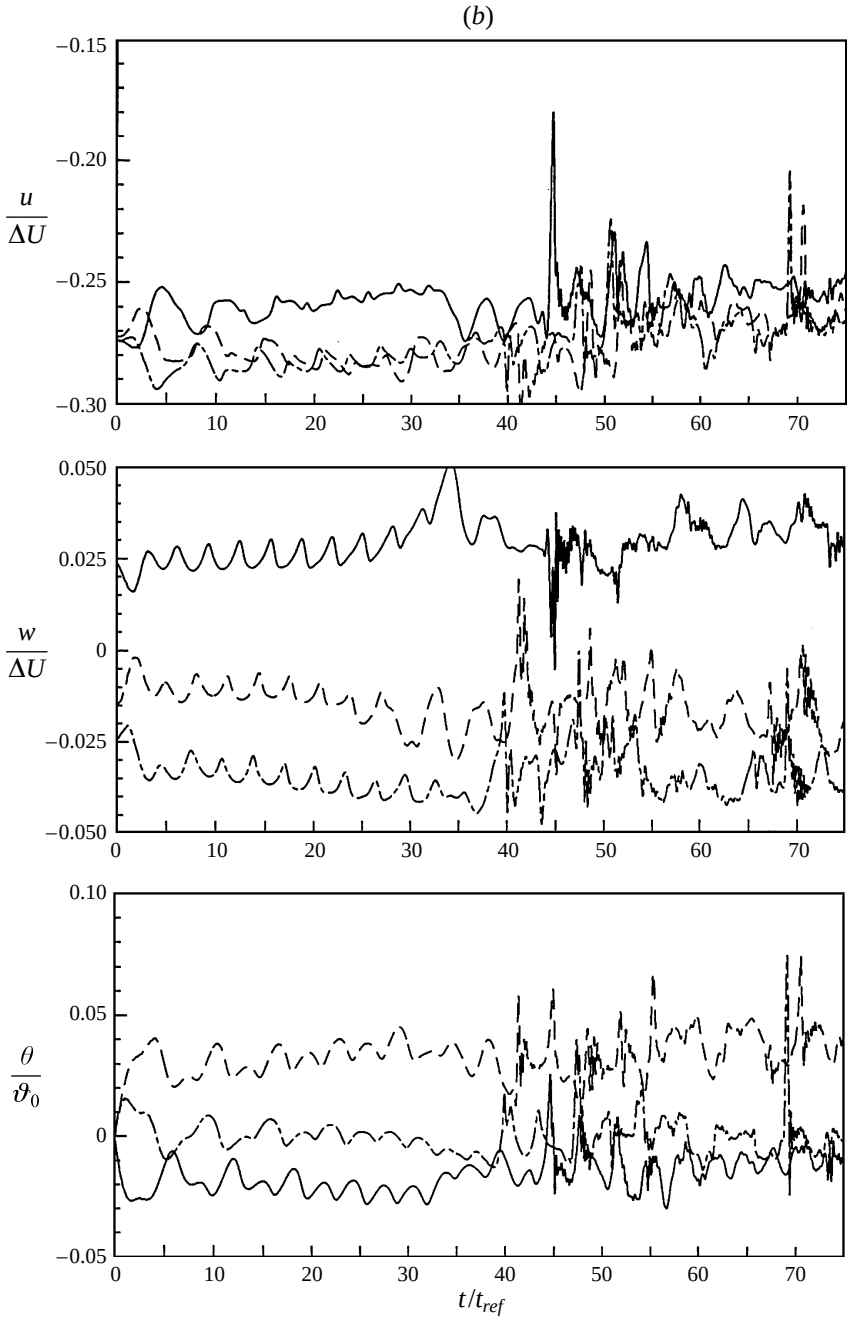

FIGURE 6. (*a*) Time-series of local and instantaneous values of the streamwise and vertical velocity u and w, and of the temperature θ. Data are taken every timestep of the numerical model at three x-positions in the plane $y = 0$ and at $\eta \approx 0.46$. The respective z-positions of the three curves are $x/\lambda = 0.2$: ——— at $z = 0.462$; $x/\lambda = 0.6$: – – – – at $z = 0.4894$; $x/\lambda = 0.8$: – · – · – at $z = 0.462$. (*b*) As (*a*) but for $\eta \approx 0.21$: $x/\lambda = 0.2$: ——— at $z = 0.232$; $x/\lambda = 0.6$: – – – – at $z = 0.205$; $x/\lambda = 0.8$: – · – · – at $z = 0.232$.

at this vertical level. It reaches larger values at lower altitudes, up to $\delta U = 0.12$ at $\eta \approx 0.38$. At $t \approx 10$, the horizontal velocity at $x = 0.2\,\lambda$ also increases because the region of strong vertical transport of horizontal momentum has been shifted in the negative x-direction. At the same horizontal position, u undergoes large-amplitude oscillations during the period ($t \approx 35$–50) when the momentum-flux barrier has been penetrated by streamwise vortices and turbulence production has become maximum underneath. Similar temporal oscillations occur in the thermal field: strong negative temperature fluctuations arise simultaneously with large u-values indicating the small-scale shear-induced secondary overturning rolls. In the late stage, the u-time-series at this vertical level show wave-like oscillations around the level $u = 0$ caused by the advection of overturning rolls at lower altitudes. The most distinct signal in the w- and θ-fields is the strong oscillation in the primary unstable layer ($x = 0.8\,\lambda$) due to the convective instability. Figure 6 (*a*) also displays an abrupt temperature change at $t = 16.5$ due to the spontaneous and explosive breaking. Afterwards, the temperature fluctuation increases rapidly but smoothly. However, it is disrupted again at $t = 17$ by another eruption from the convectively unstable flow. The vertical velocity field changes smoothly and follows the temperature field temporally. At later times, the large-amplitude oscillations caused by the breaking are damped but are excited again when turbulence is produced at lower levels.

In contrast to $\eta \approx 0.46$, the time series at lower altitude $\eta \approx 0.21$ show turbulence after a wavy period lasting up to $t \approx 35$ (see figure 6 *b*). In the following, the discussion will be confined to the curve $x = 0.2\,\lambda$ because the other horizontal positions behave similarly. Initially, the local velocity u is negative ($u \approx -0.27$). The smaller deposit of wave momentum causes a smaller rate of velocity change at this level compared to $\eta \approx 0.46$. During the early stage, periodic oscillations with a nearly constant period $T \approx 3.1$ or a frequency of $\omega = 2$ appear as the dominant signal in all curves. For a fluid at rest, the maximum frequency allowed for internal gravity waves is the Brunt–Väisälä frequency $N = Ri_B^{1/2} \approx 1$. However, at the bottom surface, perturbations of frequency $k_x U \approx 2$ are excited as seen in the time-series. Therefore, the observed frequency is just twice N. The intrinsic frequency of the gravity waves is $\hat{\omega} = \omega - k_x u(\eta)$. At $\eta \approx 0.21$ and for all heights where $\gamma < 1$, $\hat{\omega}$ is less than N, as expected. The amplitude of the velocity and temperature oscillations is large compared to the level $\eta \approx 0.46$. Interestingly, the magnitude of the temperature amplitude alternates periodically in time up to $t = 20$ (see figure 6 *b*). The period between the respective maxima is approximately 6. If we take a mean velocity $U_0 = -0.26$ at this level and if we assume that the whole flow structures remain unchanged in time, then they return at a fixed position every $\lambda/U_0 = 1.5625/0.26 \approx 6$. Hence, the origin of these returning patterns is simply their advection by the mean flow. During the breaking, the time-series are characterized by intermittent high-frequency oscillations and smooth (laminar) periods. The occurrence of the turbulent periods is caused by the isolated regions of negative Richardson number in the cores of the overturning rolls.

4. Reynolds number influence

In Dörnbrack *et al.* (1995) it was shown that for sufficient viscous damping three-dimensional turbulent convective instabilities are more easily suppressed than two-dimensional overturning. Using only constant diffusivities instead of the subgrid-scale model of (2.7), no turbulent motions were found. Mixing takes place as a quasi-periodic rolling-up of isentropes and the flow permanently contains overturning rolls. On the other hand, in runs where $\nu_M = 0$ and $\nu_{turb} \neq 0$, overturning waves immediately

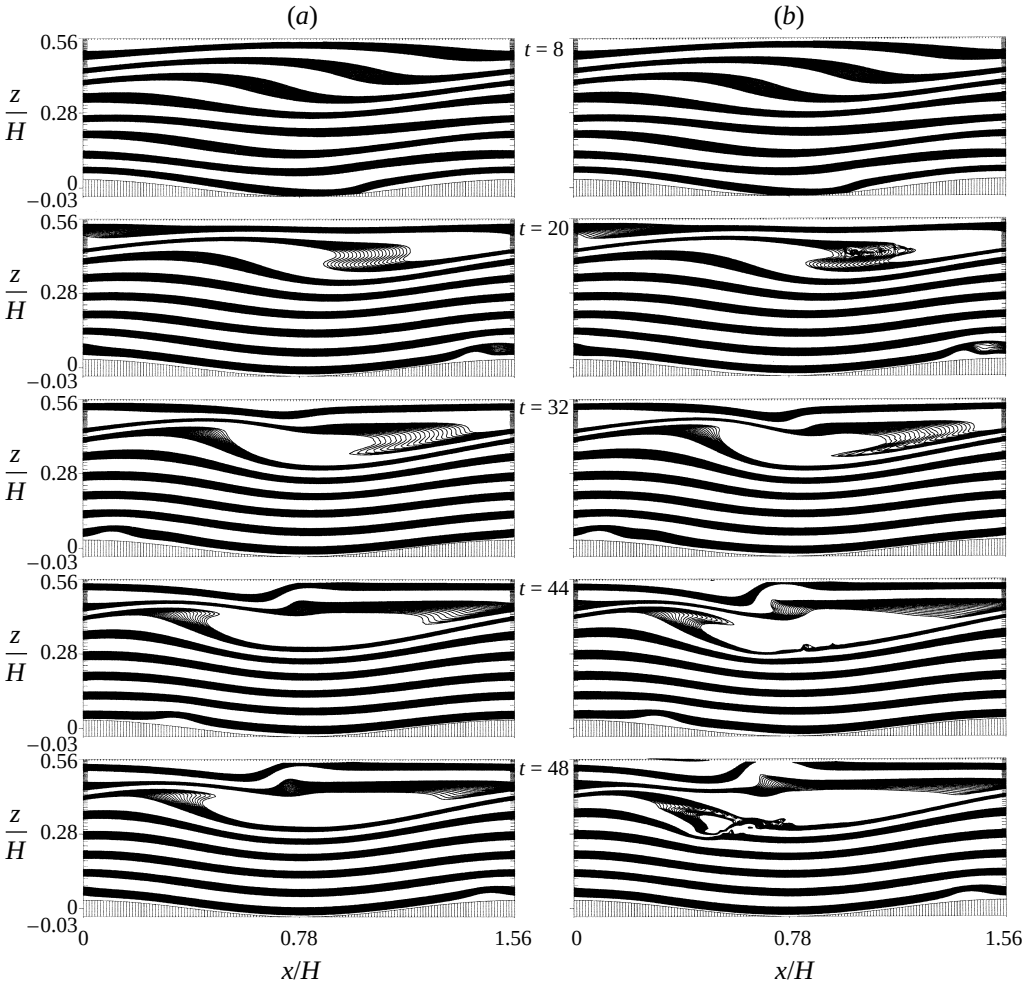

FIGURE 7. Thermal structure of flows at Reynolds numbers $Re = 2 \times 10^4$ (*a*) and $Re = 3 \times 10^4$ (*b*). The contour line spacing is as in figure 2 (*a*).

break down into three-dimensional turbulence after reaching the point of instability. Mixing processes occur much faster than in the former case. In this section, the effect of changing the Reynolds number is investigated using the subgrid-scale viscosity introduced by (2.7). To this end, figure 7 juxtaposes the flow evolutions of numerical experiments for the choice of $Re = 2 \times 10^4$ and $Re = 3 \times 10^4$. Besides the shorter simulation time of 50 dimensionless time units and the Reynolds number, all other parameters remain unchanged.

The formation of an essentially convectively unstable layer is revealed in both simulations at $t \approx 20$. Whereas the isentropes remain smooth for $Re = 2 \times 10^4$, the onset of the convective breakdown wrinkles the previously smooth contours for the lower viscosity case. At earlier times, the local flow below the critical level increases by the same value $\delta U \approx 0.06$ for all Reynolds numbers considered in this study. However, only turbulent velocity components exist for $Re \geqslant 3 \times 10^4$ because the reduced viscosity allows for the growth of three-dimensional instabilities. Sensitivity studies revealed that the impetus of explosive wave breakdown depends on

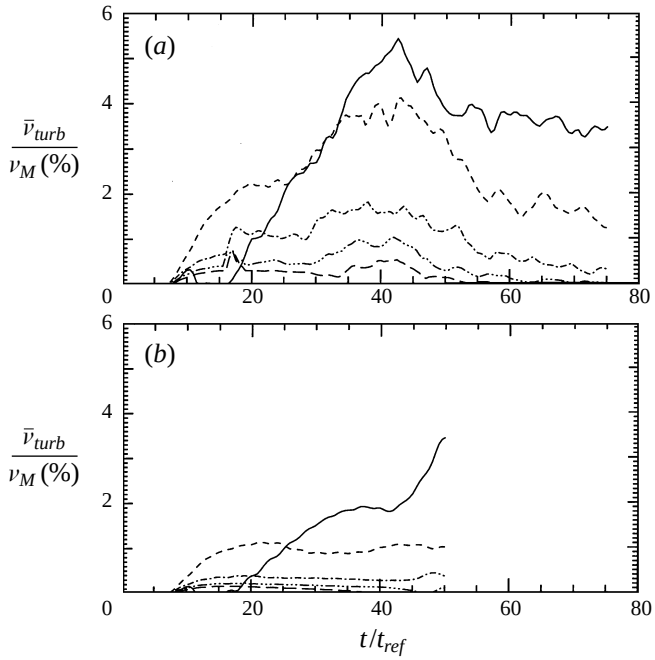

FIGURE 8. Temporal evolution of the ratio $\overline{\nu}_{turb}/\nu_M$ for (*a*) $Re = 5 \cdot 10^4$ and (*b*) $Re = 3 \times 10^4$. The curves are averages over horizontal planes of constant $\eta = 0.35$ (————), 0.39 (- - - - -), 0.42 (– · – · –), 0.45 (– · · · – · · · –), 0.47 (— — —).

the Prandtl number: temperature fluctuations initiated by the convective breakdown become larger as a result of a reduced thermal conductivity $1/RePr$.

At later times ($t > 20$), the flow remains essentially two-dimensional for higher viscosity and approaches an equilibrium state where the convectively unstable region is maintained without turbulence production. This structure resembles the two-dimensional findings of Winters & d'Asaro (1989) who observed that wave overturning persists for more than ten buoyancy periods without breaking. The low-viscosity case produces a horizontally extended turbulent mixed layer as described for case $Re = 5 \times 10^4$ in § 3. Note, that the acceleration for positions to the left of the trough ($x < \lambda/2$) depends strongly on Re. For $Re = 5 \times 10^4$ the local flow accelerates up to $\delta U \approx 0.22$ whereas for $Re = 2 \times 10^4$ it reaches only $\delta U \approx 0.12$ at $t = 45$. Hence, the lower the viscosity, the higher the momentum transfer to the local mean flow and, finally, the earlier the breakdown and the transition to a turbulent mixed layer.

The flow-independent part ν_M dominates the total viscosity as shown in figure 8. There, the ratio of horizontally averaged turbulent to kinematic viscosity $\overline{\nu}_{turb}/\nu_M$ is shown for $Re = 3 \times 10^4$ and 5×10^4 at selected altitudes up to the critical level. Although the ratio is much smaller for $Re = 3 \times 10^4$ compared to $Re = 5 \times 10^4$, their temporal behaviours are similar. The turbulent viscosity ν_{turb} is different from zero only when the local Richardson number drops below the critical value and if the shear perturbation S' has grown in the region below the critical level. The retarded increase of the ratio at different vertical levels shows the downward spread of the mixed region. The ratio $\overline{\nu}_{turb}/\nu_M$ never exceeds 6%, i.e. the additional turbulent contribution enhances the total viscosity only slightly. However, during a breaking event, instantaneous values of ν_{turb} attain 20% to 30% of ν_M. These are restricted to

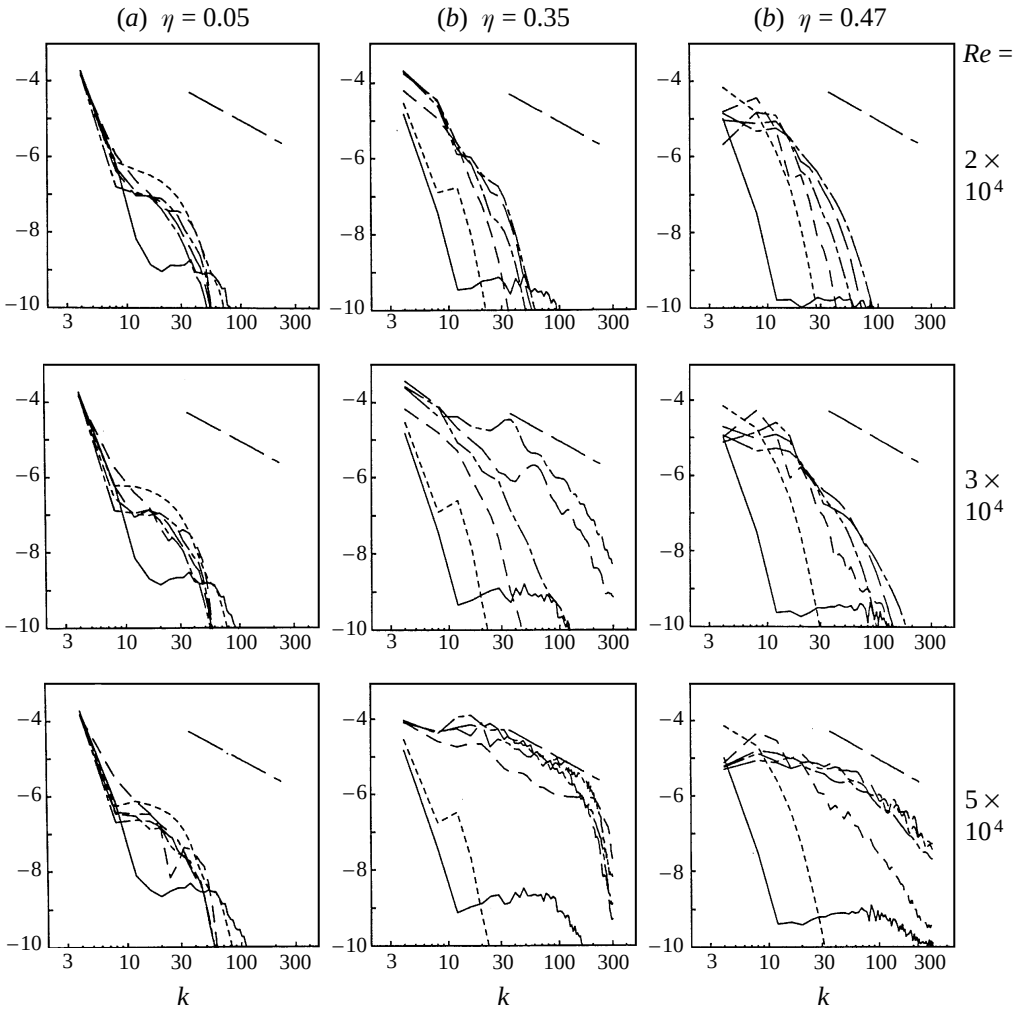

FIGURE 9. Spectra of the perturbation kinetic energy $\Phi(k)$ as function of the horizontal wavenumber $k = nk_x$ with $1 \leqslant n \leqslant nx/2$ where $k_x = 2\pi/\lambda = 4.02$. The spectra are averages at different vertical levels (*a*) $\eta = 0.05$, (*b*) 0.35, (*c*) 0.47 and they comprise both wavy and turbulent motion components. The Reynolds numbers are 2×10^4 (top), 3×10^4 (middle), and 5×10^4 (bottom). The curves denote the times $t = 2$ (————), 14 (- - - - - -), 26 (– – – –), 38 (– · – · –), 44 (— — —), and 50 (— · — · —). The long dashed line marks the $k^{-5/3}$-slope of the inertial subrange.

regions of intense turbulent mixing in the inner part of overturning waves. Hence, the overall flow evolution is not sensitive to the formulation of ν_{turb} in (2.8).

Figure 9 shows the power spectra of kinetic energy as a function of the horizontal wavenumber k. For all Reynolds numbers, the spectra are essentially the same near the bottom surface. There most of the kinetic energy is at the smallest wavenumber $k_x = 4.02$ due to the forcing by the sinusoidal terrain. At later times, higher modes are excited but their spectral amplitude remains three orders of magnitude below the dominating mode at k_x.

At $\eta = 0.35$, the spectral characteristic changes dramatically with Re and in time. For $Re = 2 \times 10^4$, the peak value at k_x increases in time by an order of magnitude and, simultaneously, higher modes are supplied with energy. However, their spectral

amplitude remains negligibly small compared to that of k_x. The temporal change of $\Phi(k)$ for $Re = 3 \times 10^4$ reveals a gradual energy injection at smaller scales so that the dominant scale of disturbances is larger than $0.2\,\lambda$. In the period $t = 44$–50, the spectral energy grows rapidly at small scales due to small-scale overturning and turbulence.

A dramatic increase in the energy for wavenumbers larger than $k \approx 10$ (or wavelengths less than $0.4\,\lambda$) characterizes the spectra for $Re = 5 \times 10^4$ during the period $t = 14$–26. For $t \geqslant 38$, a classical turbulence profile is obtained at this vertical level: most of the kinetic energy is contained in scales between $0.15\,\lambda$ and $0.35\,\lambda$ ($k \approx 10$–30). This scale roughly corresponds to the diameter of the energetic secondary rolls. The spectral amplitude of $\Phi(k)$ slopes according to $k^{-5/3}$ for the wavenumber $30 < k < 200$ (scales down to $0.02\,\lambda$). For smaller scales ($k > 200$), dissipation dominates the k^{-x}-slope, where $x \geqslant 7$. The turbulent Reynolds number is defined as $Re_{turb} = (L_{turb}/\eta_{turb})^{4/3}$. In the mixed layer the integral scale L_{turb} and the microscale η_{turb} of turbulence can be estimated from the spectra in figure 9. L_{turb} is the scale of energy injection into the inertial subrange ($\approx 0.2\,\lambda$) and $\eta_{turb} \approx 0.016\,\lambda$ is the scale where $\Phi(k)$ becomes proportional to k^{-7}, i.e. the turbulent Reynolds number of the flow is estimated to be $Re_{turb} \approx 30$. Subsequently, the dissipation range expands towards smaller wavenumbers (up to $k = 100$) while the large-scale peak of the inertial subrange remains at $k \approx 10$–30. Consequently, the turbulent Reynolds number decreases to $Re_{turb} \approx 10$ during the latter stage of flow evolution.

In order to complete the picture, $\Phi(k)$-spectra on the plane $\eta = 0.47$ are displayed in figure 9(*c*). Initially, this plane is located directly beneath the critical level. For times when the critical level has descended below $\eta = 0.47$, spectral amplitude decreases. The spectra are similarly shaped but their amplitude is about an order of magnitude smaller compared to those at the lower level $\eta = 0.35$.

5. Energetics and mixing efficiency

The budgets of domain-averaged total energy per unit mass E_T and of turbulent kinetic energy E_K'' for case $Re = 5 \times 10^4$ were computed. At $t = 0$, the total potential energy is set to zero and only deviations in E_P' from this equilibrium state are considered. Then, the total initial energy can be estimated by the kinetic energy from the prescribed velocity field $U(z)$ alone:

$$E_T(0) = E_K(0) \approx \frac{1}{2}\int_0^1 U^2(z)\,\mathrm{d}z = \frac{1}{2}\int_0^1 (z-0.5)^2,\mathrm{d}z = \frac{1}{24}. \tag{5.1}$$

For $t > 0$, the total kinetic energy per unit mass $E_K = 0.5\,{}^V\overline{u_i^2}$ (${}^V\overline{f}(t)$ denotes the domain average of a quantity f) can be divided into three parts according to (A 3) in the Appendix: $E_K = E_K^M + \tilde{E}_K + E_K''$, where the mean kinetic energy E_K^M and the wavy and turbulent parts are calculated by means of

$$E_K^M = \tfrac{1}{2}\,{}^V\overline{\overline{u_i}^2}, \quad \tilde{E}_K = \tfrac{1}{2}\,{}^V\overline{\tilde{u}_i^2}, \quad E_K'' = \tfrac{1}{2}\,{}^V\overline{u''^2}, \tag{5.2}$$

where $E_K' = \tilde{E}_K + E_K''$. By analogy, the potential energy perturbation E_P' can be divided into available potential energy $\tilde{E}_P = \frac{1}{2}Ri_B\,{}^V\overline{\tilde{\vartheta}^2}$ and into the potential energy $E_P'' = \frac{1}{2}Ri_B\,{}^V\overline{\vartheta''^2}$ associated with turbulent mixing. Table 1 lists instantaneous values of E_K^M, E_K', E_P' and of the accumulated energy loss by mechanical dissipation $\mathscr{L}$. The

t	$E_K^M/10^{-2}$	$E'_K/10^{-4}$	$E'_P/10^{-4}$	$\mathscr{L}/10^{-4}$	$\mu = \dfrac{\Delta E''_P}{\Delta E_K}$ (%)	$\dfrac{E''_P}{E''_K}$	$\dfrac{E_T - E_T(0)}{E_T(0)}$ (%)
2	4.130	1.74	0.76	0.005	0.0	0.00	−0.28
8	4.125	2.24	1.12	0.054	0.0	0.00	−0.18
20	4.109	2.64	1.28	0.390	1.2	0.11	−0.35
32	4.082	3.47	1.46	1.285	1.8	0.15	−0.54
44	4.047	3.53	0.94	3.549	3.7	0.24	−0.96
56	4.008	2.81	0.83	5.397	0.9	0.19	−1.66
68	3.986	2.62	0.69	6.469	0.6	0.22	−2.03
74	3.976	2.53	0.64	6.908	0.4	0.18	−2.20

TABLE 1. Instantaneous values of the mean kinetic energy E_K^M, the perturbation kinetic and potential energy E'_K and E'_P, of the accumulated energy loss $\mathscr{L}$, the mixing efficiency μ, the ratio of E''_P to E''_K, and the relative error of the numerical model.

accumulated energy loss is estimated by

$$\mathscr{L}(t = n\Delta t) = \sum_{j=1}^{n} {}^{V}\overline{\epsilon'_K(j\Delta t)}\Delta t, \quad n = 1, \ldots, 150, \tag{5.3}$$

where n is number of time steps and $\Delta t = 0.5$ is the time step. The dissipation rate is calculated by

$$\epsilon'_K = (\nu_M + \nu_{turb}) \frac{1}{V^2} \left(\frac{\partial}{\partial \overline{x}^r} \, VG^{dr} \, u'_d \right)^2. \tag{5.4}$$

Ideally the total energy of the fluid in the computational domain $E_T(t) = E_K + E'_P + \mathscr{L}$ should remain constant throughout the calculations. The last column of table 1 lists the relative difference between the actual total energy $E_T(t)$ and its initial value $E_T(0)$. The 2% loss of energy up to $t = 74$ is caused by numerical and thermal dissipation which are not accounted for in estimating $\mathscr{L}$. Nevertheless, the numerical code preserves energy fairly well.

The mean kinetic energy E_K^M of the flow decreases by 5% up to $t = 74$ because the accelerated flow beneath the critical level reduces both the magnitude of the negative u-velocity and $\overline{u_i}^2$ itself. This mean kinetic energy $E_K^M(t) - E_K(0)$ is transferred into perturbed motions, i.e. into E'_K and E'_P, and finally into the energy loss by dissipation (see table 1). During the first stage of flow evolution, the vertical displacements of isentropes from their initial horizontal configuration increase the total available potential energy $\tilde{E}_P$ and kinetic energy $\tilde{E}_K$. Therefore, the time-series of $\tilde{E}_K$ and $\tilde{E}_P$ (which are identical to E'_K and E'_P in this period, respectively) are dominated by periodic oscillations where maxima in E'_K correspond to minima in E'_P (see figure 10). The perturbation energies E'_K and E'_P continue to increase until $t \approx 35$ when mixing becomes dominant. At this time, approximately 30% of $E_K^M(t) - E_K(0)$ has been transferred into perturbation kinetic energy (20% in the wavy, 10% in the turbulent component), 10% into perturbation potential energy, and the rest has been dissipated. Subsequently, the perturbation energies decrease and remain constant up to the end of the simulation.

During the second stage of flow evolution, the turbulent energy E''_K as well as the dissipation (the slope of $\mathscr{L}$ is proportional to ϵ'_K) increase due to turbulent mixing beneath the critical level. In contrast to $\tilde{E}_K$ and $\tilde{E}_P$, the time histories of E''_K and E''_P increase monotonically and possess no temporal oscillations. The ratio of E''_P to

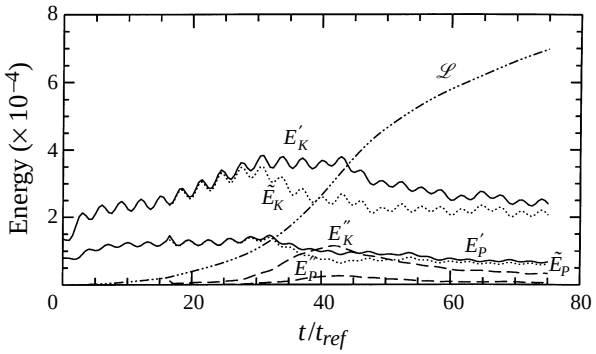

FIGURE 10. Time-series of volume-averaged perturbation kinetic and potential energies $E'_K = \tilde{E}_K + E''_K$ and $E'_P = \tilde{E}_P + E''_P$ for $Re = 5 \times 10^4$. The wavy motion components are marked by dotted lines, the turbulent components by dashed lines. The accumulated loss of kinetic energy through mechanical dissipation is denoted by $\mathscr{D}$.

the turbulent kinetic energy E''_K becomes maximum 24% during the intense mixing period (see table 1).

The potential energy E''_P increases because turbulent mixing takes place beneath the critical level. The ratio of the potential energy increase $\Delta E''_P$ to the kinetic energy loss ΔE_K during the mixing event determines the mixing efficiency μ, i.e. the amount of mean kinetic energy that has been spent to modify the basic-state stratification irreversibly. The kinetic energy loss during the breaking period is estimated by $\Delta E_K = E_K(t) - E_K(0)$. As expected, the mixing efficiency is zero during the first stage (up to $t \approx 17$) when only wave-like motions exist in the fluid. When wave breaking occurs, μ increases up to 4%. This implies that just this amount of mean kinetic energy is released to increase the potential energy.

The budget of the domain-averaged turbulent kinetic energy (TKE) reads

$$\frac{\partial}{\partial t} E''_K + \mathrm{ADV} = \mathrm{SP} + \mathrm{BP} + \mathrm{DIFF} - \epsilon, \tag{5.5}$$

where ADV, SP, BP, DIFF and ϵ denote the advection, the shear production, the buoyancy production, the diffusion, and the dissipation, respectively:

$$\left.\begin{aligned}
\mathrm{ADV} &= \frac{1}{V} \overline{{}^{V} \frac{\partial}{\partial \overline{x}^d} \left(V G^{dj} u_j E''_K \right)}, \\
\mathrm{DIFF} &= \frac{1}{V} \overline{{}^{V} \frac{\partial}{\partial \overline{x}^d} \left(G^{dj} V J_j \right)} \quad \text{where} \quad J_j = \overline{{}^{V} u''_j \left(E''_K + p''/\rho_0 \right)}, \\
\mathrm{SP} &= -\overline{u''_i u''_j} \frac{1}{V} \overline{{}^{V} \frac{\partial}{\partial \overline{x}^d} \left(V G^{dj} u_j \right)}, \\
\mathrm{BP} &= Ri_B \overline{{}^{V} w'' \theta''}, \\
\epsilon &= (\nu_{turb} + \nu_M) \frac{1}{V^2} \overline{{}^{V} \frac{\partial}{\partial \overline{x}^r} \left(V G^{dr} u''_d \right)^2}.
\end{aligned}\right\} \tag{5.6}$$

Time-series of the individual terms of (5.5) are plotted in figure 11. Except for the residual determination of $(\partial/\partial t)E''_K$, all other terms are calculated directly according to (5.6). As expected, advection and diffusion equal zero. In terms of TKE and in accordance with results of § 3, the flow regime can be characterized in three stages.

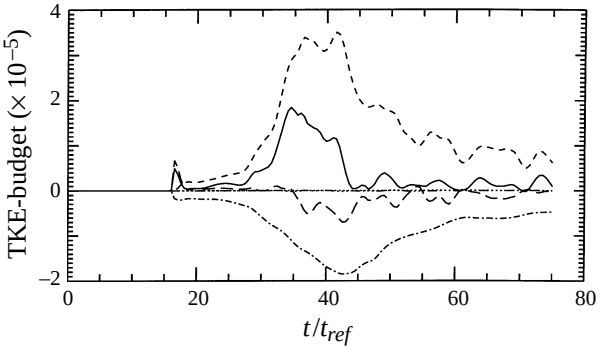

FIGURE 11. Time-series of the volume-averaged terms of the balance equation of the turbulent kinetic energy for $Re = 5 \times 10^4$. The individual curves denote: local change $\partial E_K''/\partial t$ (————), advection (· · · · · ·), diffusion (- · · · - · · · -), shear production (- - - - - -), buoyancy production (— — —), and dissipation $-\epsilon$ (— · — · —). All terms are calculated directly except $\partial E_K''/\partial t$ which is residual.

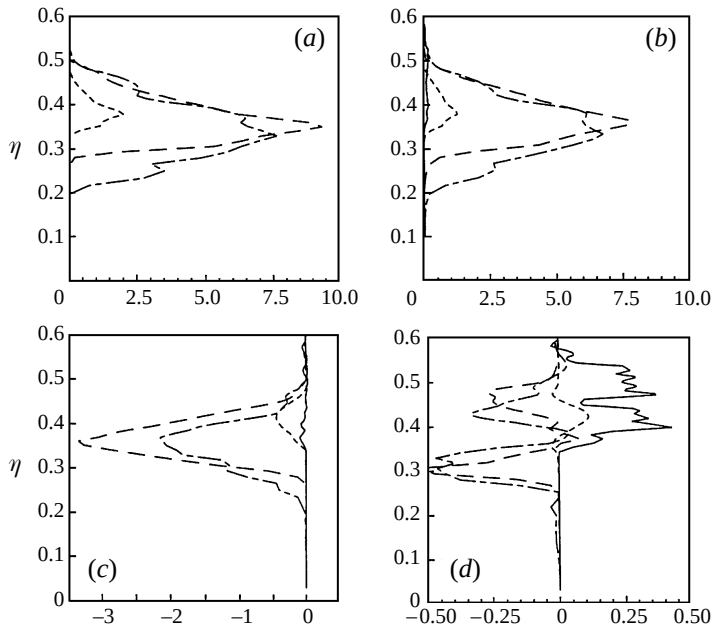

FIGURE 12. Vertical profiles of (*a*) $\overline{u''^2}$, (*b*) $\overline{E_K''}$, (*c*) $\overline{u''w''}$, and (*d*) $\overline{w''\theta''}$. The profiles are averages over planes $\eta = \text{const.}$ and the different lines at times $t = 17$ (————), 25 (- - - - - -), 36.5 (– – – –), and 43.5 (– · – · –).

In the first, essentially two-dimensional stage, the TKE is zero. TKE grows rapidly in the second phase, initially by buoyancy and later by shear production. At the end of the simulation, the positive shear production and the negative contributions due to mechanical dissipation and destruction by buoyancy are balanced and the temporal change of TKE is almost zero. The turbulent statistics is shown in figure 12. Generally, the magnitude of the turbulent variances and fluxes is much smaller than the total perturbation moments (see figure 4). For example, the ratio $\overline{u''^2}_{max}/\overline{u'^2}_{max}$ is approximately 0.05 and $\overline{u''w''}_{max}/\overline{u'w'}_{max}$ is about 0.09. The main contributions to E_K'' are due to streamwise and vertical velocity fluctuations. The lateral velocity variance

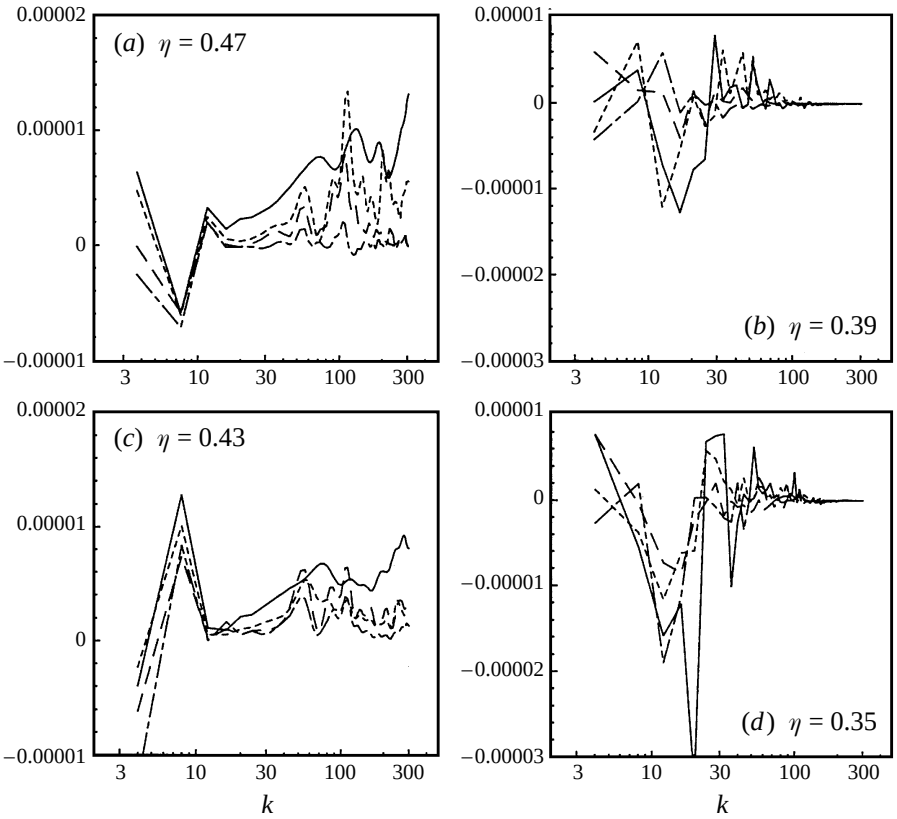

FIGURE 13. Co-spectra of the vertical heat flux $\Phi_{w'\theta'}(k)$ in an early (a,c) and a late period (b,d) of wave breaking. As in figure 9, the individual curves are averages over planes $\eta = \text{const}$. The lines are for different times: ———: 16.5 (a,c), 44 (b,d); - - - - - -: 17 (a,c), 50 (b,d); – – – –: 17.5 (a,c), 56 (b,d); – · – · –: 18 (a,c), 62 (b,d).

$\overline{v''^2} \approx \overline{v'^2}$ is approximately a factor 2 smaller than $\overline{u''^2}$. The turbulent momentum flux is always negative and counteracts the positive flux of the wave motion. This leads to a reduction of the total momentum flux down to about $z = 0.2$ as shown in figure 4.

The vertical turbulent heat flux is always negative except during the early stage of wave breaking. A negative heat flux implies that (on average) upward motions cause cooling and downward motions heating. In a thermally stably stratified environment, a positive heat flux is counter-gradient to the mean temperature gradient $\mathrm{d}\overline{\vartheta}/\mathrm{d}z$. However, this flux occurs initially in a vertically limited layer of negative $\mathrm{d}\overline{\vartheta}/\mathrm{d}z$, hence $-\overline{w''\theta''}$ is aligned with the mean temperature gradient and downgradient. As the $\Phi_{w'\theta'}$-spectra show pronounced maxima at high wavenumbers, small-scale motions must be responsible for the occurrence of positive $\overline{w''\theta''}$ (see figure 13 *a,b*). Note that the spectra $\Phi_{w'\theta'}$ comprehend both wavy and turbulent velocity components. However, their dominating modes are spectrally separated at this stage. The contributions of the wavy components are at small wavenumbers and appear either positive or negative depending on the respective vertical level and time. Figure 13 (*c,d*) shows $\Phi_{w'\theta'}$-spectra in the turbulent stage of flow evolution. There, the spectra are taken from lower altitudes than those in figure 13 (*a,b*). Averaged over all wavenumbers, the heat flux $\overline{w'\theta'}$ is negative. The main contribution to this flux stems from overturning rolls at wavenumbers between $k = 10$ and 30. The pronounced minima of $\Phi_{w'\theta'}$

appear at the same horizontal wavenumber as the maximum of $\Phi(k)$. Although the spectra show a positive maxima at $k \approx 30$, the turbulent contributions occurring at higher wavenumbers are nearly zero in the inertial subrange. Thus, the large eddies (overturning rolls), which are resolved in the simulation, are very efficient in downgradient transport of heat.

6. Discussion and conclusions

The three-dimensional breaking of internal gravity waves beneath a critical level has been investigated by means of high-resolution numerical simulations. For this purpose, the flow evolution of a stably stratified Boussinesq fluid confined between a wavy bottom and a plane top surface, both frictionless and adiabatic, was studied. The parameters used in the model are similar to those of Thorpe's (1981) tank experiment.

The simulation of the transition from two-dimensional wave motions to three-dimensional turbulence requires a fine spatial resolution in regions of wave instability. Therefore, the incompressible finite difference scheme using terrain-following coordinates (Krettenauer & Schumann 1992) was improved by increasing the vertical resolution near the critical level (see (2.4)). Moreover, the subgrid-scale viscosities K_M and K_H were modelled by the sum of a uniform and a flow-dependent part according to (2.7). Various Reynolds numbers have been tested to find the highest Re for which the simulation results become insensitive to further Re-changes and which minimally damp the energy at small scales. For the detailed study of the turbulent breakdown of overturning internal gravity waves $Re \approx 5 \times 10^4$ was chosen.

What are the details of breaking?

The simulated flow evolution occurs in three stages. During the first stage, the flow remains two-dimensional. The flow over the fixed wavy surface induces stationary gravity waves with respect to topography. Above the critical level, no or very small-amplitude damped wavy disturbances are observed. Below the critical level, the main effect is the persistent acceleration of the mean flow in the positive x-direction. This acceleration is opposite to the direction of $U(z)$ for $z < 0.5$. The perturbed mean flow lifts heavier fluid over lighter fluid directly beneath the critical level, whereas the mean advection in the negative x-direction at lower altitudes moves lighter fluid under heavier. Between these levels, the fluid stagnates and a convectively unstable region is formed that extends over almost one wavelength λ and has a thickness of about 0.1 the layer depth.

During the second stage, explosive convective instability leads to the first turbulent breakdown. Approximately three Brunt–Väisälä periods are required for the development of three-dimensional motions. The developing mixed layer is organized in spanwise, shear-driven overturning rolls and in counter-rotating streamwise vortices. At first, streamwise vortices derive their energy mainly from buoyancy; later shear dominates. The temporal order of instabilities found in this study agrees with predictions from linear perturbation theories by Winters & Riley (1992) and by Lin *et al.* (1993) and with numerical results of Winters & d'Asaro (1994). In contrast, Scinocca (1995) found that shear instability occurs before convective instability for mixed layers produced in overturning Kelvin–Helmholtz billows. The present results confirm Schowalter, Van Atta & Lasheras's (1994) finding that buoyancy forces contribute to an additional mechanism for the generation of streamwise vortices in the presence of stratification.

The flow in the mixed layer is random, containing vortices on a wide range of scales. The typical horizontal scale of a spanwise secondary roll is 0.2λ–$0.3\,\lambda$; the scale of the streamwise vortices is less than $0.15\,\lambda$. Caulfield & Peltier (1994) investigating stratified shear layers also found the scale of streamwise streaks of vorticity to be much smaller than the wavelength of the primary overturning structures. The lateral scale of counter-rotating streamwise vortices is smaller than the width of the computational domain and their size appears to be unaffected by it.

The final stage of flow evolution is characterized by a quasi-steady equilibrium between shear production and mechanical dissipation of turbulent kinetic energy. The final mixed layer consists of shear-induced, small-scale overturning rolls and counter-rotating streamwise vortices leading to isolated patches of turbulence embedded in a smooth flow.

What is the role of viscosity?

The results of § 4 have shown that (i) the smaller ν_M is, the earlier breaking occurs in the convectively unstably stratified regions. The flow becomes fully three-dimensional. Secondly, the smaller the viscosity, the larger the momentum deposited beneath the critical level by gravity waves and the more likely is the formation of secondary rolls and turbulent breaking by shear instability. These findings agree with results of Fritts *et al.* (1996) who found viscosity retarding instability.

What are the characteristics of turbulence generated by breaking gravity waves?

Turbulence is primarily produced by shear in the mixed layer. There, the power spectra of perturbation kinetic energy resemble classical spectra from turbulence theory. The spectral amplitude slopes according to $k^{-5/3}$ for scales smaller $0.2\,\lambda$ and down to $0.02\,\lambda$. For scales less than $0.02\,\lambda$, the spectral amplitude decreases according to k^{-x}, where $x \geqslant 7$ (dissipation range). Based on estimates of the integral scale and microscale of turbulence, the turbulent Reynolds number is computed to be approximately 30. Another remarkable result is the apparent sinking of the mixed layer due to entrainment of cold and high-momentum fluid at its lower edge. Sinking of thin turbulent layers has also been observed by radar in the free atmosphere (Sato & Woodman 1982).

How much energy of the mean flow is transferred to waves, how much to turbulence?

Although the separation into wavy and turbulent parts is controversial (see Holloway 1988; Winters *et al.* 1995), it does aid in determining the essential sources of instability energy. The mean kinetic energy of the flow decreases temporally by 5% up to $t = 74$. This mean kinetic energy is converted into perturbation kinetic and potential energy. Finally it is lost by dissipation. By the time that the flow reaches its quasi steady-state, approximately 30% of this energy has become perturbation kinetic energy (20% in the wavy, 10% in the turbulent component), 10% has become perturbation potential energy, and the remainder has been dissipated. As a check of numerical accuracy, the budget of the total kinetic energy has been computed; approximately 2% of the total energy was lost by thermal dissipation and by numerical diffusion. For internal gravity waves, the relevant dissipation process is their unstable breakdown via convective and dynamical instabilities. The mixing efficiency was calculated to be approximately 4%. Thus this small amount of mean kinetic energy is converted to potential energy and into an irreversible change of the initial thermal stratification.

Although Winters & d'Asaro (1994) and Fritts *et al.* (1996) investigated similar problems to ours, their numerical approaches (integration method, background conditions, wave forcing, and subgrid-scale modelling) are different. Winters & d'Asaro (1994), using a pseudospectral method, investigated the overturning of an initially prescribed, two-dimensional internal wave packet in an incompressible Boussinesq fluid. The ambient flow possessed constant stability and a depth-dependent shear flow with a critical level in the essentially linear segment of $U(z)$. The bulk Richardson number of 25 is higher and the spatial resolution lower compared to the present simulations. Furthermore, the classic diffusion operator was replaced by a sixth-order derivative. Fritts *et al.* (1996) investigated and compared the two- and three-dimensional breaking by integrating the compressible Eulerian equations using a spectral collocation method. Specifically, the instability structure subject to shear components transverse to the direction of wave propagation was investigated. The gravity waves were forced by a time-dependent body force that yields a wave packet containing many different frequencies and vertical wavenumbers. The viscous and diffusive effects are represented spectrally by a method described by Andreassen et al. (1994). In order to achieve a finer resolution at the locations of instability, Fritts *et al.* (1996) decomposed the model vertically into two domains and Winters & d'Asaro (1994) used up to 200 vertical levels. The instability growth and the structures of the breaking waves in this study agree fairly well with these other different numerical approaches.

This work was funded by the Deutsche Forschungsgemeinschaft (DFG) in the framework of the Schwerpunktprogramm "Grundlagen der Auswirkungen der Luft- und Raumfahrt auf die Atmosphäre".

Appendix

The classical Reynolds decomposition splits an arbitrary field f into a mean part $\overline{f}$ and a fluctuating part f' according to $f = \overline{f} + f'$. Usually, in numerical studies, the mean part of the discrete field $f_{i,j,k}(t)$ is defined as average over horizontal planes according to

$$\overline{f_k}(z,t) = \frac{1}{nx\,ny} \sum_{i,j=1}^{nx,ny} f_{i,j,k}(t). \tag{A 1}$$

Additionally, temporal averages can be used when the flow has reached a steady state. In the present study, the fluctuating part f' is split diagnostically into a wavy ($\tilde{f}$) and a turbulent (f'') component. A phase average (here, just over one wavelength)

$$\langle f \rangle_p(x,z,t) = \frac{1}{ny} \sum_{j=1}^{ny} f_{i,j,k}(t) \tag{A 2}$$

can be used to extract the wavy component $\tilde{f}$ from f according to $\tilde{f}(x,\eta,t) = \langle f \rangle_p - \overline{f}$. This sort of averaging is appropriate as long as the gravity wave excitation is homogeneous in y and the resulting flow structures are shorter than λ. Finally, the total field f consists in a mean part $\overline{f}$, a wavy ($\tilde{f}$), and a turbulent (f'') part according to

$$f = \overline{f} + \tilde{f} + f'' \quad \text{where} \quad f''(x,y,z,t) = f - \overline{f} - \tilde{f}. \tag{A 3}$$

This sort of decomposition was introduced by Hussain & Reynolds (1970) and has been formerly used *inter alia* by Fritts, Isler & Andreassen (1994) and Fritts *et al.* (1996).

REFERENCES

Andreassen, Ø., Wasberg, C. E., Fritts, D. C. & Isler, J. R. 1994 Gravity breaking in two and three dimensions. 1. Model description and comparison of two-dimensional evolutions. *J. Geophys. Res.* **99**, 8095–8108.

Bacmeister, J. T., Newman, P. A., Gary, B. L. & Chan, K. R. 1994 An algorithm for forcasting mountain wave-related turbulence in the stratosphere. *Weather and Forcasting* **9**, 241–253.

Baines, P. G. 1995 *Topographic Effects in Stratified Flows.* Cambridge University Press, 482 pp.

Booker, J. R. & Bretherton, F. P. 1967 The critical layer for internal gravity waves in a shear flow. *J. Fluid Mech.* **27**, 513–539.

Broad, A. S. 1995 Linear theory of momentum fluxes in 3-D flows with turning of the mean wind with height. *Q. J. R. Met. Soc.* **121**, 1891–1902.

Carslaw, K. S., Wirth, M., Tsias, A., Luo, B. P., Dörnbrack, A., Leutbecher, M., Volkert, H., Renger, W., Bacmeister, J. T. & Peter, T. 1998*a* Particle microphysics and chemistry in remotely observed mountain polar stratospheric clouds. *J. Geophys. Res.* **103**, 5785–5796.

Carslaw, K. S., Wirth, M., Tsias, A., Luo, B. P., Dörnbrack, A., Leutbecher, M., Volkert, H., Renger, W., Bacmeister, J. T., Reimer, E. & Peter, T. 1998*b* Increased stratospheric ozone depletion due to mountain-induced atmospheric waves. *Nature* **391**, 675–678.

Caulfield, C. P. & Peltier, W. R. 1994 Three dimensionalization of the stratified mixing layer. *Phys. Fluids* **6**, 3803–3805.

Delisi, D. P. & Dunkerton, T. J. 1989 Laboratory observations of gravity wave critical-layer flows. *Pure Appl. Geophys.* **130**, 445–461.

Dörnbrack, A. & Dürbeck, T. 1998 Turbulent dispersion of aircraft exhausts in regions of breaking gravity waves. *Atmos. Env.* **32**, 3105–3112.

Dörnbrack, A., Gerz, T. & Schumann, U. 1995 Turbulent breaking of overturning gravity waves below a critical level. *Appl. Sci. Res.* **54**, 163–176.

Dörnbrack, A. & Nappo, C. J. 1997 A note on the application of linear wave theory at a critical level. *Boundary Layer Met.* **82**, 399–416.

Dunkerton, T. J & Robins, R. E. 1992 Radiating and nonradiating modes of secondary instability in a gravity-wave critical-level. *J. Atmos. Sci.* **49**, 2546–2559.

Eliassen, A. & Palm, E. 1960 On the transfer of energy in stationary mountain waves. *Geofysiske Publikasjoner* **XXII**, 1–23.

Fritts, D. C. 1982 The transient critical-level interaction in a Boussinesq fluid. *J. Geophys. Res.* **87**, 7997–8016.

Fritts, D. C., Garten, J. F. & Andreassen, Ø. 1996 Wave breaking and transition to turbulence in stratified shear flows. *J. Atmos. Sci.* **53**, 1057–1085.

Fritts, D. C., Isler, J. R. & Andreassen, Ø. 1994 Gravity breaking in two and three dimensions. 2. Three-dimensional evolution and instability structure. *J. Geophys. Res.* **99**, 8109–8123.

Gill, A. E. 1982 *Atmosphere-Ocean Dynamics.* Academic.

Grubišić, V. & Smolarkiewicz, P. K. 1997 The effect of critical levels on 3D orographic flows: linear regime. *J. Atmos. Sci.* **54**, 1943–1960.

Holloway, G. 1988 The buoyancy flux from internal gravity wave breaking. *Dyn. Atmos. Oceans* **12**, 107–125.

Hussain, A. K. M. F. & Reynolds, W. C. 1970 The mechanics of an organized wave in turbulent shear flow. *J. Fluid Mech.* **41**, 241–258.

Kim, Y.-J. & Arakawa, A. 1995 Improvement of orographic gravity wave parametrization using a mesoscale gravity wave model. *J. Atmos. Sci.* **52**, 1875–1902.

Koop, C. G. & McGee, B. 1986 Measurements of internal gravity waves in a continiously stratified shear flow. *J. Fluid Mech.* **172**, 453–480.

Krettenauer, K. & Schumann, U. 1992 Numerical simulation of turbulent convection over wavy terrain. *J. Fluid Mech.* **237**, 261–299.

Lilly, D. K. 1962 On the numerical simulation of buoyant convection. *Tellus* **14**, 148–172.

Lin, C.-L., Ferzinger, J. H., Koseff, J. R. & Monismith, S. G. 1993 Simulation and stability of two-dimensional internal gravity waves in a stratified shear flow. *Dyn. Atmos. Oceans* **19**, 325–366.

Peter, T., Müller, R., Pawson, S. & Volkert, H. 1995 POLECAT: Preparatory and modelling studies. *Phys. Chem. Earth* **20**, 109–121.

Sato, K. & Woodman, R. F. 1982 Fine altitude resolution radar observations of stratospheric layers by the Arecibo 430 MHz radar. *J. Atmos. Sci.* **39**, 2546–2552.

Schilling, V. & Etling, D. 1996 Vertical mixing of passive scalars owing to breaking gravity waves. *Dyn. Atmos. Oceans* **23**, 371–378.

Schowalter, D. G., Van Atta C. W. & Lasheras, J. C. 1994 A study of streamwise vortex structure in a stratified shear layer. *J. Fluid Mech.* **281**, 247–291.

Schumann, U. 1975 Subgrid scale model of finite difference simulations of turbulent flows in plane channels and annuli. *J. Comput. Phys.* **18**, 376–404.

Schumann, U., Konopka, P., Baumann, R., Busen, R., Gerz, T, Schlager, H., Schulte, P. & Volkert, H. 1995 Estimate of diffusion parameters of aircraft exhaust plumes near the tropopause from nitric oxide and turbulence measurements. *J. Geophys. Res.* **100**, 14147–14162.

Scinocca, J. F. 1995 The mixing of mass and momentum by Kelvin–Helmholtz billows. *J. Atmos. Sci.* **52**, 2509–2530.

Scorer, R. S. 1949 Theory of lee waves over mountains. *Q. J. R. Met. Soc.* **75**, 41–56.

Shutts, G. 1995 Gravity-wave drag parametrization over complex terrain: The effect of critical-level absorption in directional wind-shear. *Q. J. R. Met. Soc.* **121**, 1005–1021.

Smith, R. B. 1979 The influence of mountains on the atmosphere. *Adv. Geophys.* **21**, 87–230.

Thorpe, S. A. 1981 An experimental study of critical layers. *J. Fluid Mech.* **103**, 321–344.

Winters, K. B. & D'Asaro, E. A. 1989 Two-dimensional instability of finite amplitude internal gravity wave packets near a critical level. *J. Geophys. Res.* **94**, 12709–12719.

Winters, K. B. & D'Asaro, E. A. 1994 Three-dimensional wave instability near a critical level. *J. Fluid Mech.* **272**, 255–284.

Winters, K. B., Lombard, P. N., Riley, J. J. & D'Asaro, E. A. 1995 Available potential energy and mixing in density-stratified fluids. *J. Fluid Mech.* **289**, 115–128.

Winters, K. B. & Riley, J. J. 1992 Instability of internal waves near a critical level. *Dyn. Atmos. Oceans* **16**, 249–278.

Worthington, R. M. & Thomas, L. 1996 Radar measurements of critical layer absorption in mountain waves. *Q. J. R. Met. Soc.* **122**, 1263–1282.